Quantitative live-cell imaging yields novel insight into endogenous WNT/CTNNB1 signaling dynamics

Author information

S.M.A. de Man[1], G. Zwanenburg[2,^], M.A. Hink[1,3,*,^], R. van Amerongen[1,*,^,#]

[1] Swammerdam Institute for Life Sciences, Section of Molecular Cytology, University of Amsterdam, Amsterdam, the Netherlands.

[2] Swammerdam Institute for Life Sciences, Biosystems Data Analysis Group, University of Amsterdam, Amsterdam, The Netherlands

[3] Swammerdam Institute for Life Sciences, van Leeuwenhoek Centre for Advanced Microscopy, University of Amsterdam, Amsterdam, the Netherlands.

* These authors contributed equally

^ corresponding authors: r.vanamerongen@uva.nl (RvA), m.a.hink@uva.nl (MAH), g.zwanenburg@uva.nl (GZ)

Twitter: @wntlab

Abstract

WNT/CTNNB1 signaling regulates tissue development and homeostasis in all multicellular animals. Multiple aspects of the underlying molecular mechanism remain poorly understood and critical information on endogenous WNT/CTNNB1 signaling dynamics is missing. Here we combine CRISPR/Cas9-mediated genome editing and quantitative live-cell microscopy to measure diffusion characteristics of fluorescently tagged, endogenous CTNNB1 in human cells with high spatiotemporal resolution. State-of-the-art functional imaging reveals that both in the absence and presence of WNT, a substantial fraction of CTNNB1 resides in slow-diffusing complexes in the cytoplasm and that WNT stimulation changes their identity. We also measure the concentration of complexed and free CTNNB1 in both the cytoplasm and the nucleus before and after WNT stimulation, and use these parameters to build a minimal computational model of WNT/CTNNB1 signaling. Our work reveals that WNT regulates the dynamic distribution of CTNNB1 across different functional pools by modulating the destruction complex, nucleocytoplasmic shuttling and nuclear retention.

Introduction

WNT signaling is one of the most ancient pattern-forming cell signaling cascades. It drives many biological processes from the onset of embryogenesis until adulthood in all multicellular animals (reviewed in van Amerongen and Nusse, 2009; Holstein, 2012; Loh et al., 2016). WNT signaling remains important throughout the lifespan of the organism and controls stem cell maintenance in many mammalian tissues, including the breast, intestine and skin (Barker et al., 2007; Lim et al., 2013; van Amerongen, Bowman, & Nusse, 2012). Disruption of the pathway causes disease, with hyperactivation being a frequent event in human colorectal and other cancers (reviewed in Nusse and Clevers, 2017; Polakis, 2000; Wiese et al., 2018; Zhan et al., 2017).

The key regulatory event in WNT/CTNNB1 signaling (traditionally known as 'canonical WNT signaling') is the accumulation and nuclear translocation of the transcriptional co-activator beta-catenin (CTNNB1). In the absence of WNT signaling, rapid turnover by the so-called destruction complex maintains low levels of CTNNB1 (Figure 1A). The destruction complex consists of the scaffold proteins APC and AXIN, which bind CTNNB1, and the serine/threonine kinases CSNK1 and GSK3, which subsequently phosphorylate residues S45, T41, S37 and S33 (Amit et al., 2002; C. Liu et al., 2002). This primes CTNNB1 for ubiquitination by E3 Ubiquitin Protein Ligase BTRC and subsequent proteasomal degradation (Aberle, Bauer, Stappert, Kispert, & Kemler, 1997; Latres, Chiaur, & Pagano, 1999). In the current working model for WNT/CTNNB1 signaling, binding of WNT ligands to the FZD/LRP receptor complex sequesters and inhibits the destruction complex at the membrane in a process that involves DVL (Bilic et al., 2007; Schwarz-Romond et al., 2007). This allows newly synthesized CTNNB1 to accumulate (Figure 1B). Upon stimulation, CTNNB1 also translocates to the nucleus, where CTNNB1 binds to TCF/LEF transcription factors to regulate target gene transcription as part of a larger

53 transcriptional complex (Behrens et al., 1996; Fiedler et al., 2015; Molenaar et al., 1996; van
54 Tienen, Mieszczanek, Fiedler, Rutherford, & Bienz, 2017).

55 The working model for WNT/CTNNB1 signaling described above, is the result of almost 40
56 years of research. The use of traditional genetic and biochemical approaches has allowed
57 identification of the core players, as well as dissection of the main signaling events. However,
58 multiple aspects of WNT/CTNNB1 signaling remain poorly understood. For instance the exact
59 molecular composition and mechanism for inhibition of the destruction complex remain
60 unclear (reviewed in Tortelote et al., 2017), and how WNT/CTNNB1 signaling regulates the
61 subcellular distribution of CTNNB1 requires further scrutiny.

62 Most biochemical techniques lead to loss of spatial information and averaging of cell-to-cell
63 heterogeneity, since proteins are extracted from their cellular context. Additionally, temporal
64 information is usually limited to intervals of several minutes or hours. Live-cell microscopy
65 offers better spatiotemporal resolution. However, currently many of these studies are
66 conducted by overexpressing the protein(s) of interest. This can severely affect activation,
67 localization and complex formation (T. J. Gibson, Seiler, & Veitia, 2013; Mahen et al., 2014).
68 Although stabilization of CTNNB1 by WNT signaling has been extensively studied, there are
69 very few studies on the spatiotemporal dynamics of this process especially at the endogenous
70 level (Chhabra, Liu, Goh, Kong, & Warmflash, 2019; Massey et al., 2019; Rim, Kinney, & Nusse,
71 2020).

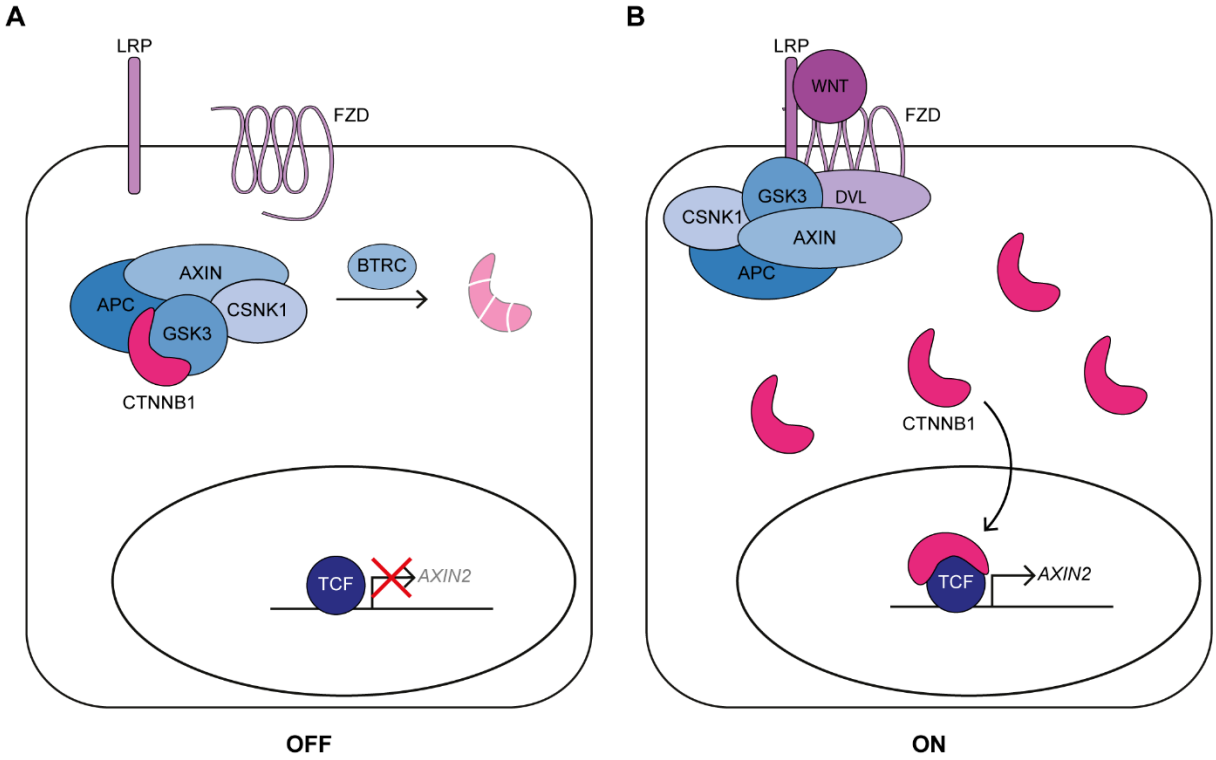

Figure 1: Current model of the WNT/CTNNB1 pathway. A) In the absence of WNT ligands, free cytoplasmic CTNNB1 is captured by the destruction complex (or "degradosome") consisting of AXIN, APC, CSNK1 and GSK3, where it is sequentially phosphorylated by the latter two kinases. This phosphorylation triggers ubiquitination by BTRC and subsequent proteasomal degradation. As a result, levels of CTNNB1 are kept low in both the cytoplasm and the nucleus. B) Binding of the WNT protein to the FZD and LRP receptors inhibits the destruction complex. This process is mediated by DVL and is thought to sequester the destruction complex to the membrane (also known as the "signalosome"). CTNNB1 accumulates in the cytoplasm and subsequently translocates to the nucleus, where it promotes the transcription of target genes, such as AXIN2, as a co-activator of TCF/LEF transcription factors. This transcriptional complex contains multiple other partners and is also termed the "enhanceosome". Note that CTNNB1 also plays a structural role at the membrane in adherens junctions (not depicted).

Here we use CRISPR/Cas9 mediated genome editing in haploid cells to generate clonal cell lines that express fluorescently tagged CTNNB1. Using confocal imaging and automated cell segmentation we quantify the dynamic subcellular increase of endogenous CTNNB1 upon WNT stimulation. Moreover, using Fluorescence Correlation Spectroscopy (FCS) and Number and Brightness (N&B) analysis we measure the mobility and concentration of CTNNB1, providing information on CTNNB1 containing complexes in the cytoplasm and nucleus. Finally, we use these parameters to construct a novel computational model of WNT/CTNNB1 signaling. Our combined approach offers new insight into the dynamic regulation of CTNNB1 in mammalian cells through modulation of the destruction complex as well as nucleocytoplasmic shuttling and nuclear retention.

Results

Generation of clonal HAP1$^{SGFP2\text{-}CTNNB1}$ cell lines

To be able to visualize and quantify the spatiotemporal dynamics of WNT/CTNNB1 signaling at the endogenous level, we fluorescently tagged CTNNB1 in mammalian cells using CRISPR/Cas9 mediated homology directed repair (Ran et al., 2013) (Figure 2). To preserve the existing (epi)genetic control mechanisms of *CTNNB1* expression, only the coding sequence for SGFP2, a monomeric, bright and photostable green fluorescent protein (G.-J. Kremers, Goedhart, van den Heuvel, Gerritsen, & Gadella, 2007), was seamlessly inserted at the starting ATG of the *CTNNB1* coding sequence in HAP1 cells (Figure 2A, Figure 2 supplement 2A). HAP1 is a near-haploid and WNT responsive cell line (Andersson et al., 1987; Carette et al., 2011; Kotecki, Reddy, & Cochran, 1999; Lebensohn et al., 2016). By using haploid cells, we could ensure homozygous tagging of *CTNNB1* (Figure 2B), thus overcoming the limitations of polyploid cell lines where genome editing often results in a combination of correctly and incorrectly edited alleles (Canaj et al., 2019).

To obtain clonal cell lines with the desired modification, single SGFP2-positive cells were isolated by FACS sorting (Figure 2C-E). Because HAP1 cells have the tendency to become diploid or polyploid over time (Essletzbichler et al., 2014; Yaguchi et al., 2018), we used a gating strategy to specifically select for haploid cells (Figure 2 supplement 1). Genome editing of wild-type HAP1 (HAP1^{WT}) cells with a targeting gRNA and the *SGFP2-CTNNB1* repair construct resulted in a slight increase in fluorescence for a small population (0.2%) of cells compared to non-repaired control cells (Figure 2C-D). Treatment of these cells with CHIR99021, a potent and selective GSK3 inhibitor (Bain et al., 2007), resulted in an increase of the green fluorescence intensity (Figure 2E), but not the absolute number of positive events. The responsiveness to CHIR99021 provided a strong indication that these fluorescent

117 events corresponded to HAP1 cells in which the *SGFP2* sequence was successfully knocked
118 into the endogenous *CTNNB1* locus (HAP1$^{SGFP2\text{-}CTNNB1}$).

119 PCR based screening confirmed that 22/23 single-cell sorted clones indeed showed an
120 integration of the expected size at the *CTNNB1* locus. Complete sequence coverage of the
121 insertion site in exon 2 was obtained for 9/11 sequenced clones, of which 8 showed the
122 desired repair, and 1 clone showed an additional point mutation in the repaired locus. Sanger
123 sequencing results around the *SGFP2* integration site are shown for three correctly targeted
124 HAP1$^{SGFP2\text{-}CTNNB1}$ clones from three independent transfections, which were used for further
125 experiments (Figure 2 supplement 2B-C). Thus, while scarless tagging of endogenous genes in
126 HAP1 cells is relatively cumbersome (only 0.2% gated events), the desired repair occurs with
127 almost 90% efficiency within this population.

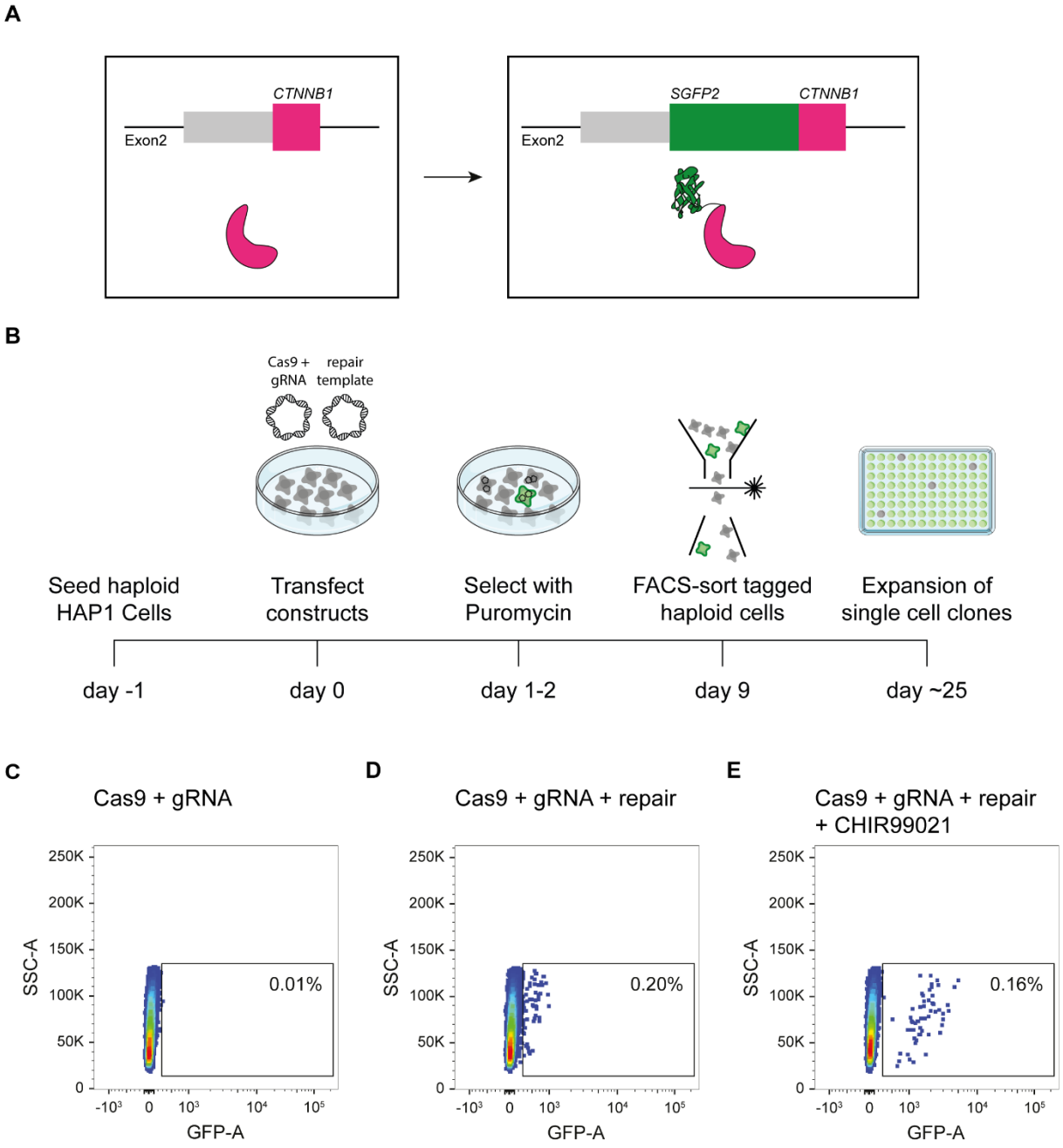

Figure2: Generation of HAP1$^{SGFP2\text{-}CTNNB1}$ cell lines. A) Cartoon depicting exon 2 of the *CTNNB1* locus, which contains the start codon, and the CTNNB1 protein before (left) and after (right) introduction of the SGFP2 by CRISPR/Cas9 mediated homology directed repair. B) Schematic of the experimental workflow and timeline for generating HAP1$^{SGFP2\text{-}CTNNB1}$ clones. Cas9, gRNA and repair templates are transfected as plasmids. The repair template contains the coding sequence of SGFP2 surrounded by 800 bp homology arms on either side and lacks the gRNA recognition site (see supplement 2 of this figure). A short puromycin selection step is included from 24-48 hours after transfection to enrich for transfected cells. Haploid, GFP-positive cells are sorted and single cell clones are expanded for further analysis. C-E) FACS plots illustrating control (C) and SGFP2-CTNNB1 tagged cells (D-E). C) Cells transfected with Cas9 and gRNA in the absence of a repair template were used to set the gate for SGFP2-positive events. D) A small population of cells expressing low levels of SGFP2 can be detected when cells are transfected with Cas9, gRNA and repair template. E) Treatment of cells similar to those depicted in (D) with 8µM CHIR99021 does not change the amount of cells that are SGFP2 positive, but increases the SFP2 signal, most likely reflecting an increase in SGFP2-tagged beta catenin levels on a per cell basis and supporting the notion that the gated events indeed represent successfully tagged cells.

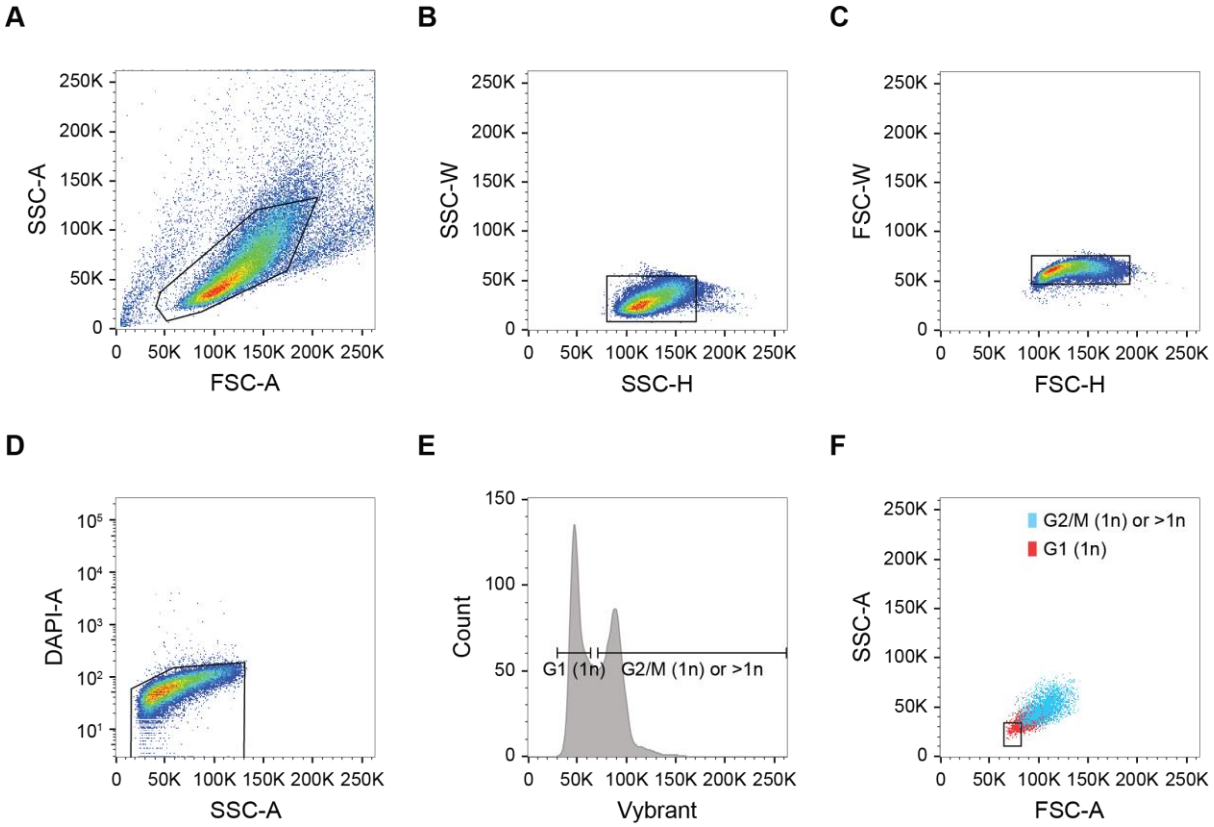

Figure 2 – supplement 1: FACS Gating strategy for haploid HAP1 cells. A-C) Single-cell gating based on forward scatter (FSC) and side scatter (SSC). D) Live cell gating based on DAPI exclusion. E-F) Haploid cell sorting based on Vibrant live-cell DNA dye. E) Haploid cell cycle profile. Only cells in G1 can be confidently identified as haploid (1n). The second peak contains both G2/M haploid cells, as well as diploid (2n) and polyploid events. Of note, the depicted HAP1^{WT} population is mainly haploid. F) Back-gating of the haploid G1 population from E onto the forward and side scatter plot. A stringent gate is set based on cell size to ensure only G1 (1n) cells qualify for sorting.

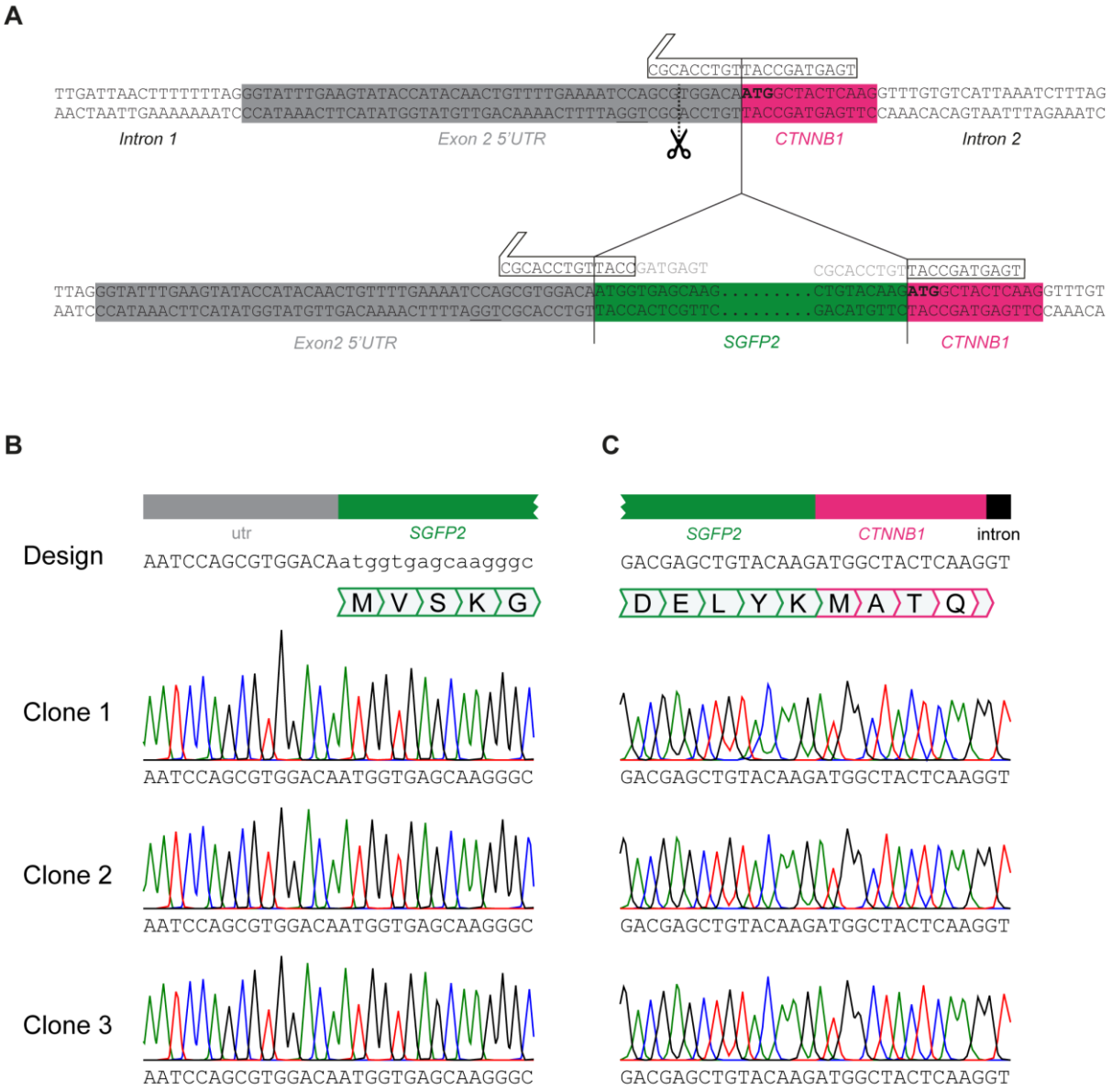

Figure 2 – supplement 2: *SGFP2-CTNNB1* locus A) Detailed view of *CTNNB1* exon 2 depicting gRNA design relative to the wildtype (top) and repaired (bottom) CTNNB1 allele. Note that the repair template contains the same sequence as the repaired allele depicted here. CTNNB1 sequences are shown in capital letters, SGFP2 sequences shown in lowercase. 5' UTR, *SGFP2* and *CTNNB1* and intron regions are indicated below the colored boxes. The gRNA (white arrow box above sequence) overlaps the start codon (depicted in bold), resulting in a Cas9-mediated double-strand break in the 5'UTR (predicted cut site indicated by dotted line and scissor, PAM site underlined). After successful homologous recombination, most of the gRNA binding site is destroyed, thus minimizing the chance of cutting the repair template or re-cutting the repaired allele. B-C) Sequencing of three independent HAP1$^{SGFP2\text{-}CTNNB1}$ clones on the 5' (B) and the 3' (C) end of *SGFP2* integration in exon 2 of *CTNNB1*. Sanger sequencing of the endogenous *CTNNB1* locus of clone 1, clone 2 and clone 3 shows an exact match to the design and thus correct homology directed repair.

Functional validation of the HAP1$^{SGFP2\text{-}CTNNB1}$ knock-in allele

To verify that the SGFP2 tag did not interfere with CTNNB1 function, three clonal HAP1$^{SGFP2\text{-}CTNNB1}$ cell lines were further characterized using established experimental readouts for WNT/CTNNB1 signaling (Figure 3 and Figure 3 supplement). Western blot analysis confirmed that the HAP1$^{SGFP2\text{-}CTNNB1}$ clones did not contain any untagged CTNNB1 but only expressed the fusion protein, which ran at the expected height (~27 kDa above the wild-type CTNNB1, Figure 3A). Moreover, in response to CHIR99021 treatment the total levels of SGFP2-CTNNB1 in tagged cell lines increased to the same extent as wild-type CTNNB1 in untagged cells, as detected with both CTNNB1 and GFP antibodies (Figure 3A-B). To examine if SGFP2-CTNNB1 was able to promote TCF/LEF transcriptional activity, we measured the induction of the TCF/LEF-responsive MegaTopflash luciferase reporter (Hu et al., 2007). Stimulation of the WNT/CTNNB1 pathway with CHIR99021 resulted in a similar range of reporter gene activation in the three tagged clones and parental HAP1 cells (Figure 3C). Induction of the universal WNT/CTNNB1 target gene *AXIN2* (Lustig et al., 2002) was also comparable across wildtype and tagged cells (Figure 3D). Finally, we visualized the subcellular accumulation of SGFP2-CTNNB1 accumulation after WNT/CTNNB1 pathway activation. While untreated cells mainly show membrane localization of CTNNB1, treatment with purified WNT3A protein (Figure 3E) and CHIR99021 (Figure 3 supplement 1E) increased SGFP2-CTNNB1 levels in the cytoplasmic and nucleus.

Taken together, WNT-responsive changes in CTNNB1 levels and localization and activity are preserved after CRISPR/Cas9 mediated homozygous tagging of CTNNB1. Although there is some variation between the three clones with respect to CTNNB1 stabilization and target gene activation, this is likely due to the sub-cloning of these cell lines rather than the targeting

per se. Based on the combined characterization results, we selected clone 2 for more extensive functional imaging experiments and analyses.

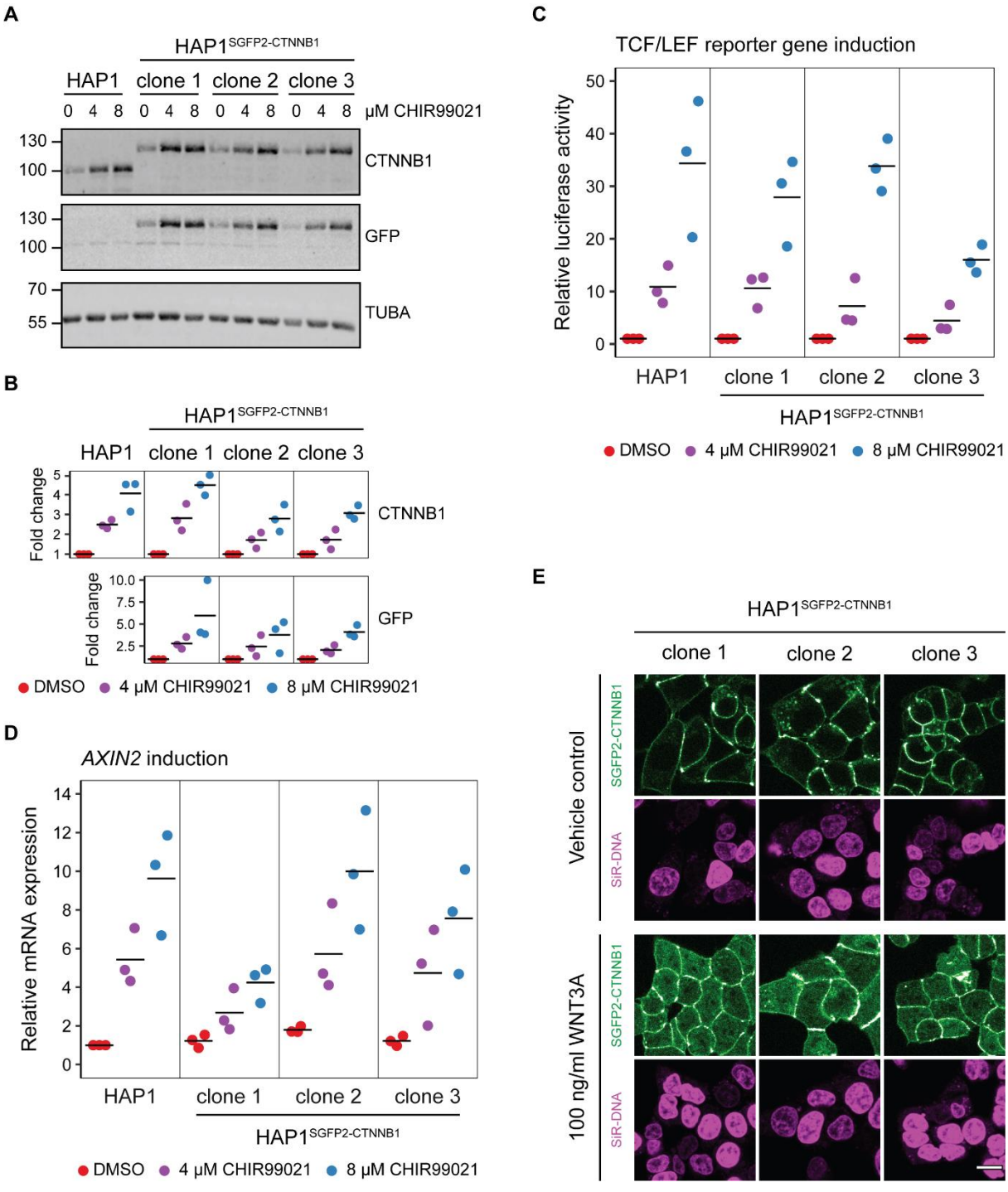

Figure3: Functional validation of three independent HAP1$^{SGFP2\text{-}CTNNB1}$ clones. A) Western blot, showing CTNNB1 (HAP1^{WT}) and SGFP2-CTNNB1 (HAP1$^{SGFP2\text{-}CTNNB1}$ clone 1, 2 and 3) accumulation in response to CHIR99021 treatment. All panels are from one blot that was cut at the 70 kDa mark and was stained with secondary antibodies with different fluorophores for detection. Top: HAP1^{WT} cells express CTNNB1 at the expected wild-type size. Each of the three clonal HAP1$^{SGFP2\text{-}CTNNB1}$ cell lines only express the larger, SGFP2-tagged form of CTNNB1. Middle: Only the tagged clones express the SGFP2-CTNNB1 fusion protein, as detected with an anti-GFP antibody at the same height. Bottom: alpha-Tubulin (TUBA) loading control. A representative image of n=3 independent experiments is shown. B) Quantification of Western blots from n=3 independent experiments, including the one in (A), confirming that the accumulation of CTNNB1 in response to WNT/CTNNB1 pathway

activation is comparable between HAP1^{WT} and HAP1$^{SGFP2\text{-}CTNNB1}$ cells. Horizontal bar indicates the mean. C) Graph depicting the results from a MegaTopflash dual luciferase reporter assay, showing comparable levels of TCF/LEF reporter gene activation for HAP1^{WT} and HAP1$^{SGFP2\text{-}CTNNB1}$ cells in response to CHIR99021 treatment. Data points from n=3 independent experiments are shown. Horizontal bar indicates the mean. Values are depicted relative to the DMSO control, which was set to 1 for each individual cell line. D) Graph depicting *AXIN2* mRNA induction in response to CHIR99021 treatment, demonstrating that induced expression of an endogenous target gene is comparable between HAP1^{WT} and HAP1$^{SGFP2\text{-}CTNNB1}$ cells. Data points represent n=3 independent experiments. Horizontal bar represents the mean. *HPRT* was used as a reference gene. Values are depicted relative to the HAP1^{WT} DMSO control, which was set to 1. E) Representative confocal microscopy images of the three HAP1$^{SGFP2\text{-}CTNNB1}$ clones after 4-hour vehicle control or 100ng/ml WNT3A treatment, revealing intracellular accumulation of SGFP2-CTNNB1 (green). Nuclei were counterstained with SiR-DNA dye (magenta). Scale bar is 10µm.

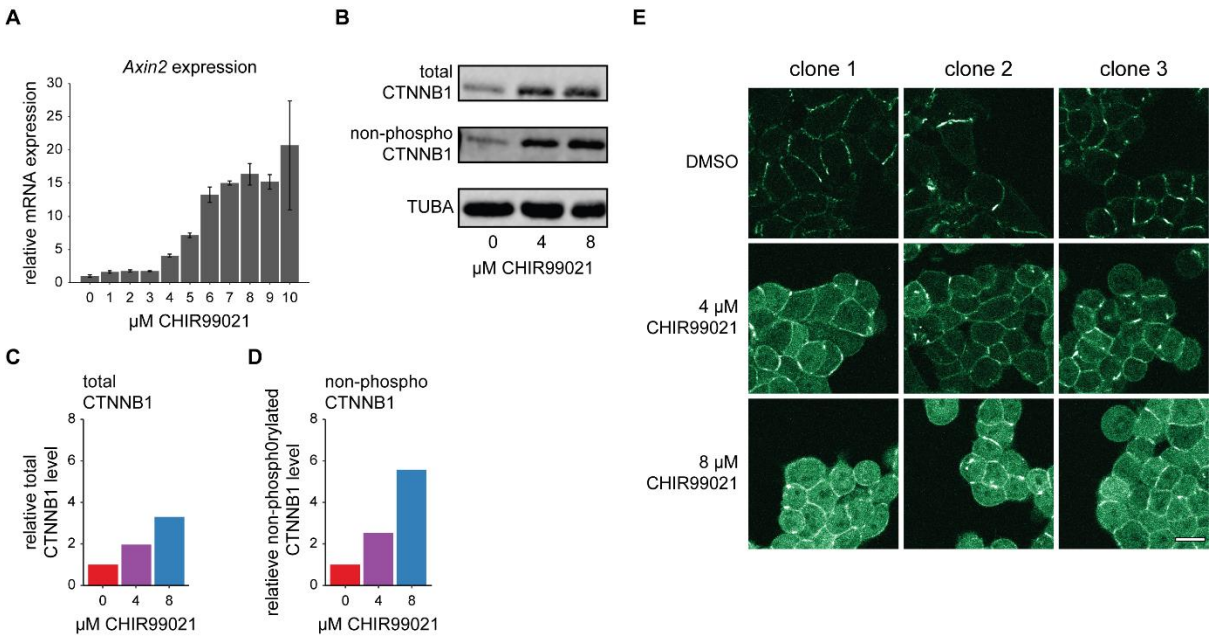

Figure 3 supplement 1: Verification of the WNT/CTNNB1 responsiveness of HAP1 cells. A) Graph depicting *AXIN2* qRT-PCR results from HAP1^{WT} cells treated with the indicated range of CHIR99021 (1-10 µM) or DMSO vehicle control (0 µM) for 24 hours. *HPRT* was used as a reference gene. Error bars represent standard deviation within technical triplicates from n=1 biological experiment. Based on this, we selected 4uM and 8 µM as intermediate and high levels of WNT/CTNNB1 pathway induction for follow up experiments. B) Western blot, showing the increase in total (top) and non-phosphorylated (i.e. active) CTNNB1 levels (middle) in response to pathway stimulation. HAP1^{WT} cells were treated for 24 hours with 4 or 8 µM CHIR99021, or DMSO vehicle control (0 µM). Alpha-Tubulin (TUBA, bottom) serves as a loading control. C-D) Quantification of the western blot from (B) depicting the relative fold change of total CTNNB1 (C) or non-phosphorylated CTNNB1 (D) to DMSO control corrected for Tubulin loading. E) Representative confocal microscopy images of three independent HAP1$^{SGFP2\text{-}CTNNB1}$ clones, treated for 24 hours with 4 or 8 µM CHIR99021, or DMSO vehicle control. Scalebar is 10 µm.

Live imaging of endogenous SGFP2-CTNNB1 during WNT pathway activation

To better understand the temporal dynamics of endogenous CTNNB1 stabilization, we performed live-cell imaging over 12 hours in HAP1$^{SGFP2\text{-}CTNNB1}$ cells (Figure 4, Supplementary Movie 1-3) with different levels of WNT stimulation. Unstimulated cells showed stable CTNNB1 localization at the cell membrane throughout the imaging time course (Figure 4A, Supplementary Movie 1). The membrane localization of CTNNB1 is consistent with its structural role in adherens junctions (Valenta, Hausmann, & Basler, 2012; Yap, Brieher, & Gumbiner, 1997), which we will not consider further in the current study. Both WNT3A and CHIR99021 treatment resulted in a heterogeneous response pattern, with some cells in the population showing a far more prominent increase in CTNNB1 levels in the cytoplasm and nucleus than others (Figure 4A, Supplementary Movie 2-3).

To quantify these dynamic changes, we developed a custom-built automated segmentation pipeline in CellProfiler™ (Figure 4B). Quantification showed that the dynamics of CTNNB1 accumulation were independent of the dose of WNT3A (Figure 4 C-D, Supplementary Movies 4-5). Treatment with 100 ng/ml WNT3A increased SGFP2-CTNNB1 fluorescence 1.74-fold (mean, 95% CI 1.73-1.76) in the cytoplasm and 3.00-fold (mean, 95% CI 2.97-3.03) in the nucleus, with similar results in the other two HAP1$^{SGFP2\text{-}CTNNB1}$ clones (Figure 4 supplement 1). Treatment with 4 µM of CHIR99021 yielded similar kinetics as WNT3A treatment (Figure 4C-D). Treatment with WNT3A and 4 µM CHIR both also resulted in a decrease of SGPF2-CTNNB1 levels toward the end of the time series. However, at the highest levels of GSK3 inhibition (8 µM CHIR99021), no plateau was reached and the levels of SGFP2-CTNNB1 continued to increase throughout the imaging time course. The fact that intracellular SGFP2-CTNNB1 levels in the 8 µM CHIR99021 condition continued to accumulate, suggests that negative feedback,

for example through *AXIN2* (Lustig et al., 2002), is overridden under these circumstances. Of note, the quantification also confirms that there is cell to cell heterogeneity in the response, regardless of whether WNT/CTNNB1 signaling is activated at the level of the receptor (WNT3A treatment) or at the level of the destruction complex (CHIR99021 treatment), as can be seen from the spread of intensities measured from individual cells (Figure 4 Supplement 2A-B).

Our quantification shows that, nuclear accumulation of CTNNB1 is favored over cytoplasmic increase (compare the slopes in Figure 4C-D). Moreover, the first significant increases in fluorescence intensity in the cytoplasm could be detected after ~45 minutes of treatment (Supplementary Movie 4, Figure 4 supplement 2C), whereas in the nucleus an increase was first after ~30 minutes (Supplementary Movie 5, Figure 4 supplement 2D). To examine the relation between the cytoplasmic and nuclear CTNNB1 pools more closely, we calculated the ratio between nuclear and cytoplasmic intensities of SGFP2-CTNNB1 (Figure 4E, Supplementary Movie 6). In untreated cells the nuclear/cytoplasmic ratio was 0.652 (mean, 95% CI 0.649-0.657), showing that SGFP2-CTNNB1 was preferentially localized to the cytoplasm (Figure 4E). For the first 3 hours after WNT3A and CHIR99021 addition, nuclear CTNNB1 levels rose considerably faster than cytoplasmic CTNNB1 levels until the nuclear/cytoplasmic ratio showed a slight nuclear enrichment of 1.08 (mean [3-5 hours] 95% CI 1.07-1.10) for 100 ng/ml WNT3A and 1.29 (mean [3-5 hours], 95% CI 1.26-1.32) for 8µM CHIR99021. This indicates that not only the turn-over, but also the subcellular localization of CTNNB1 is actively regulated both before and after WNT pathway activation.

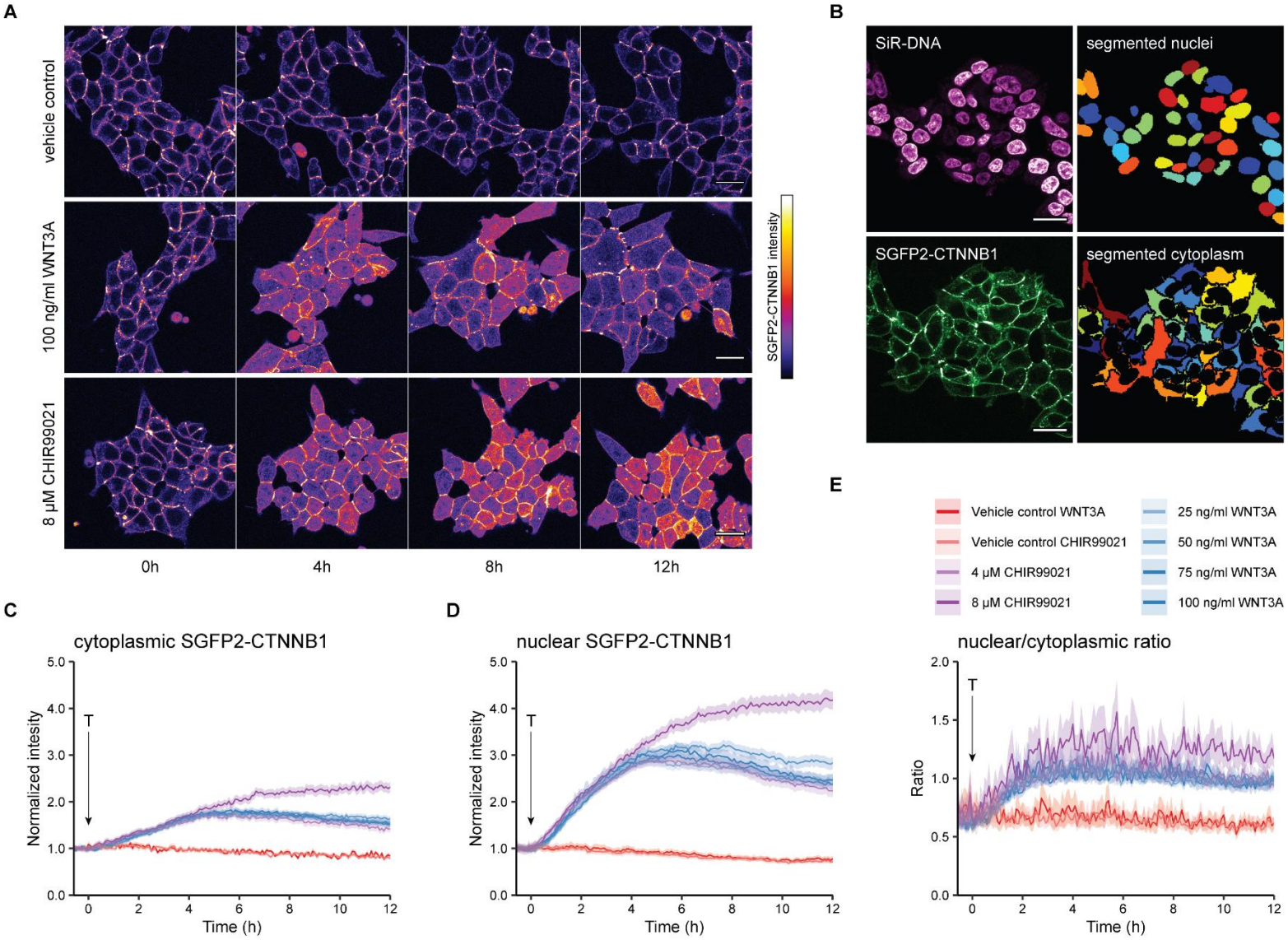
A
vehicle control
100 ng/ml WNT3A
8 µM CHIR99021
0h
4h
8h
12h
SGFP2-CTNNB1 intensity
B
SiR-DNA
segmented nuclei
SGFP2-CTNNB1
segmented cytoplasm
C
cytoplasmic SGFP2-CTNNB1
Normalized intesity
Time (h)
D
nuclear SGFP2-CTNNB1
Normalized intesity
Time (h)
E
Vehicle control WNT3A
Vehicle control CHIR99021
4 µM CHIR99021
8 µM CHIR99021
25 ng/ml WNT3A
50 ng/ml WNT3A
75 ng/ml WNT3A
100 ng/ml WNT3A
nuclear/cytoplasmic ratio
Ratio
Time (h)

255

Figure 4: Live imaging of HAP1$^{SGFP2\text{-}CTNNB1}$. A) Representative stills from confocal time-lapse experiments corresponding to Supplementary Movies 1-3, showing an increase of SGFP2-CTNNB1 after treatment with 100 ng/ml WNT3A (middle) and 8µM CHIR99021 (bottom) relative to a vehicle control (BSA) treated sample (top). Scale bar = 20 µm. B) Segmentation of nuclei (top) and cytoplasm (bottom) based in the SiR-DNA signal and SGFP2-CTNNB1 signal. Scale bar = 20µm. C-E) Quantification of time-lapse microscopy series, using the segmentation pipeline shown in (B). Arrow indicates the moment of starting the different treatments (T, see legend in E for details). C-D) Graph depicting the normalized intensity of SGFP2-CTNNB1 in the cytoplasm (C) or nucleus (D) over time. Solid lines represent the mean normalized fluorescence intensity and shading indicates the 95% confidence interval. n=155-400 cells for each condition and time point, pooled data from n=3 independent biological experiments. E) Graph depicting the nuclear/cytoplasmic ratio of SGFP2-CTNNB1 over time, calculated from raw intensity values underlying (C) and (D).

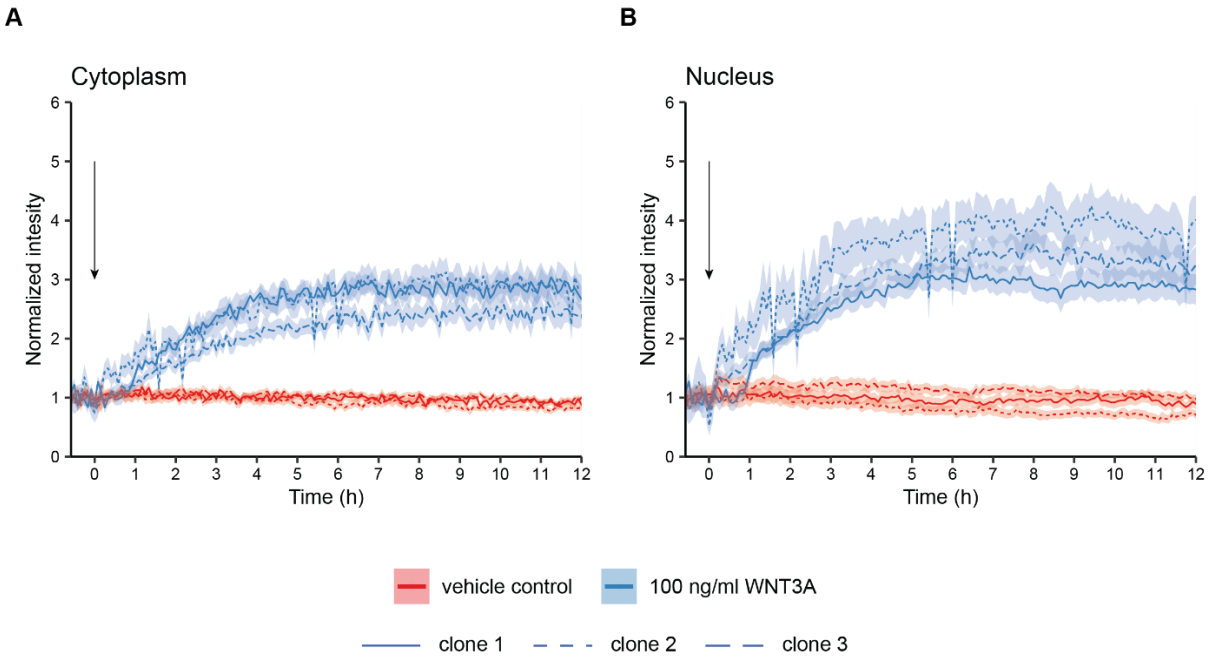

Figure 4 supplement 1: Graphs showing quantification of time-lapse microscopy experiments with three independent HAP1$^{SGFP2\text{-}CTNNB1}$ clones. Stills of this experiment are shown in Figure 3C. Segmentation was performed as described in Figure 4. Arrow indicates the moment of starting the different treatments (BSA in red or 100 ng/ml WNT3A in blue). Solid lines represent the mean normalized intensity and shading the 95% confidence interval in the cytoplasm (A) or nucleus (B). Line pattern indicates the three different clones. n=13-158 cells for each condition and time point for n=1 biological experiment.

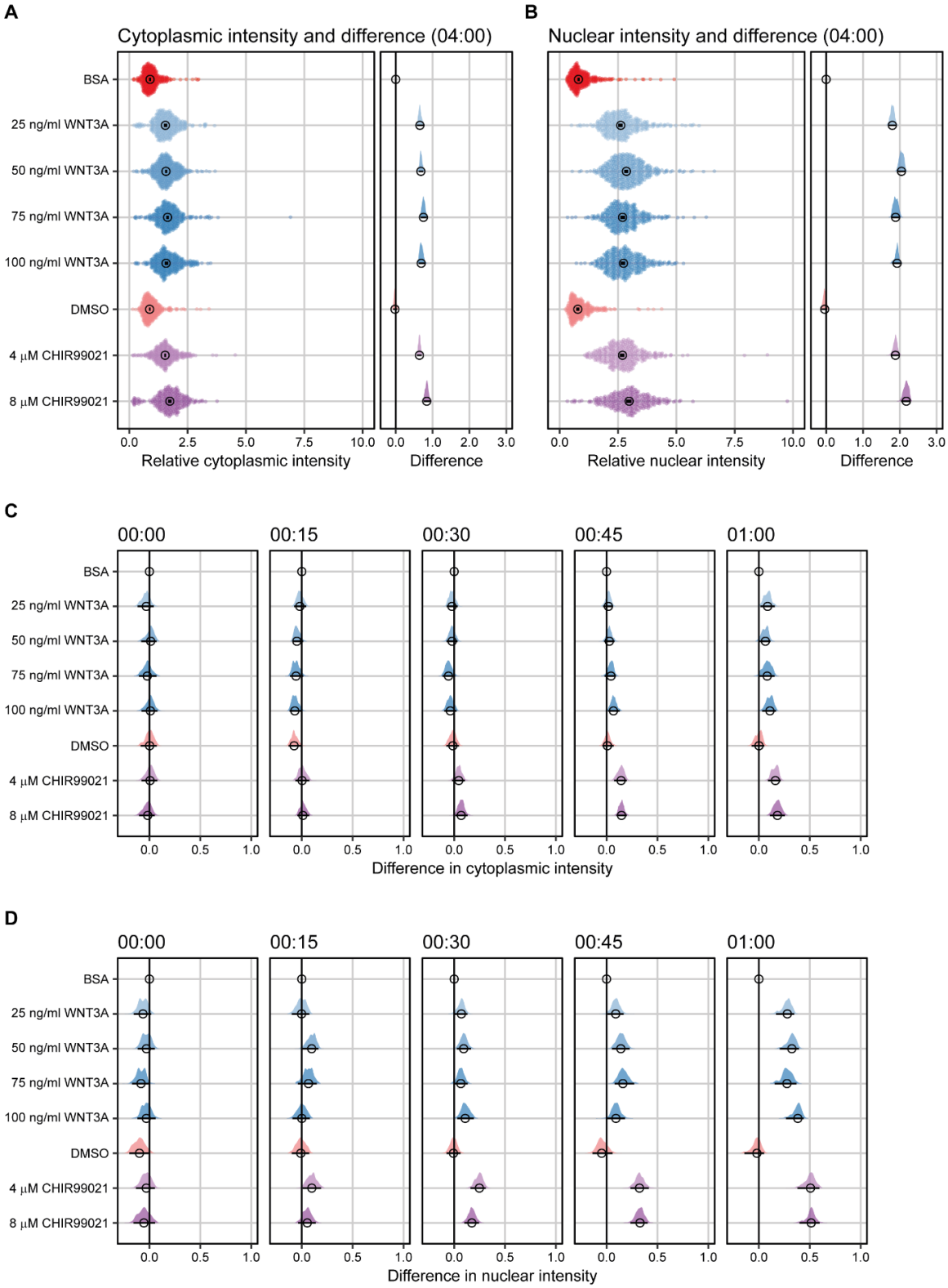

Figure 4 supplement 2 A-B) Plots depicting the relative intensity (left) and the difference in relative intensity to BSA treated cells (right) in the cytoplasm (A) and nucleus (B) after 4 hours of treatment. Circles indicate the median value and bars indicate the 95% CI. In the relative intensity plot (left) the distribution is built from individual data points in a violin-type fashion to faithfully represent the distribution of data. In the difference plot (right) the distribution of differences is represented in a half violin plot. If the 95% CI in the difference plot does not overlap the zero line, which indicates no difference, the sample is significantly different from BSA control condition. C-D) Plots depicting the difference in relative intensity in the cytoplasm (C) and nucleus (D) between the moment of addition and 1 hour of treatment. Titles indicate the time (hh:mm). The distribution of differences is represented in a half violin plot. Circles indicate the median value and bars indicate the 95% CI. If the 95% CI does not overlap the zero line, which indicates no difference, the sample is significantly different from the BSA control condition.

Establishing a fitting model for SGFP2-CTNNB1 diffusion

Having measured the relative changes in the cytoplasmic and nuclear levels of CTNNB1 in response to WNT pathway activation, we next sought to exploit our experimental system to quantify additional molecular properties of CTNNB1 in each of these subcellular compartments using Fluorescence Correlation Spectroscopy (FCS). FCS is a powerful method to measure the mobility and absolute levels of fluorescent particles in a nanomolar range, compatible with typical levels of signaling proteins in a cell (reviewed in Hink, 2014). It has for instance been used to gain insight into the assembly of DVL3 supramolecular complexes (Yokoyama, Markova, Wang, & Malbon, 2012), the endogenous concentrations and mobility of nuclear complexes (Holzmann et al., 2019; Lam et al., 2012), and most recently, to quantify ligand-receptor binding reactions in the WNT pathway (Eckert et al., 2020). In point FCS, the fluorescence intensity is measured in a single point (Figure 5 A, D-E). Diffusion of a labeled particle, in this case SGFP2-CTNNB1, causes fluctuation of the fluorescence signal over time (Figure 5B). By correlating the fluorescence intensity signal to itself over increasing time-intervals, an autocorrelation curve is generated (Figure 5C). To extract relevant biophysical parameters, such as mobility (a measure for size) and the absolute numbers of the fluorescent particles, this autocorrelation curve is fitted with an appropriate model.

We first attempted to fit the autocorrelation curves obtained with point FCS measurements of HAP1$^{SGFP2\text{-}CTNNB1}$ cells, with a model containing one single diffusion speed for SGFP2-CTNNB1. This model was unable to fit most of our data (Figure 5F). The current literature suggests that while a large portion of CTNNB1 is present as a monomer (Gottardi & Gumbiner, 2004; Maher, Mo, Flozak, Peled, & Gottardi, 2010), CTNNB1 is also present in multiprotein complexes in the cytoplasm and in the nucleus (reviewed in Gammons and Bienz, 2018).

306 Therefore, we next used a model with two diffusion components, in which the first diffusion
307 component was fixed to the diffusion speed of monomeric, unbound SGFP2-CTNNB1 (14.9
308 $\mu m^2/s$) and the second diffusion component was limited to slower speeds compatible with
309 point-FCS imaging (see materials and methods for details). This model fitted well with our
310 autocorrelation curves as obtained in both cytoplasmic and nuclear point FCS measurements
311 (Figure 5G), consistent with the presence of free monomeric CTNNB1 and larger CTNNB1
312 containing complexes in both the nucleus and cytoplasm.

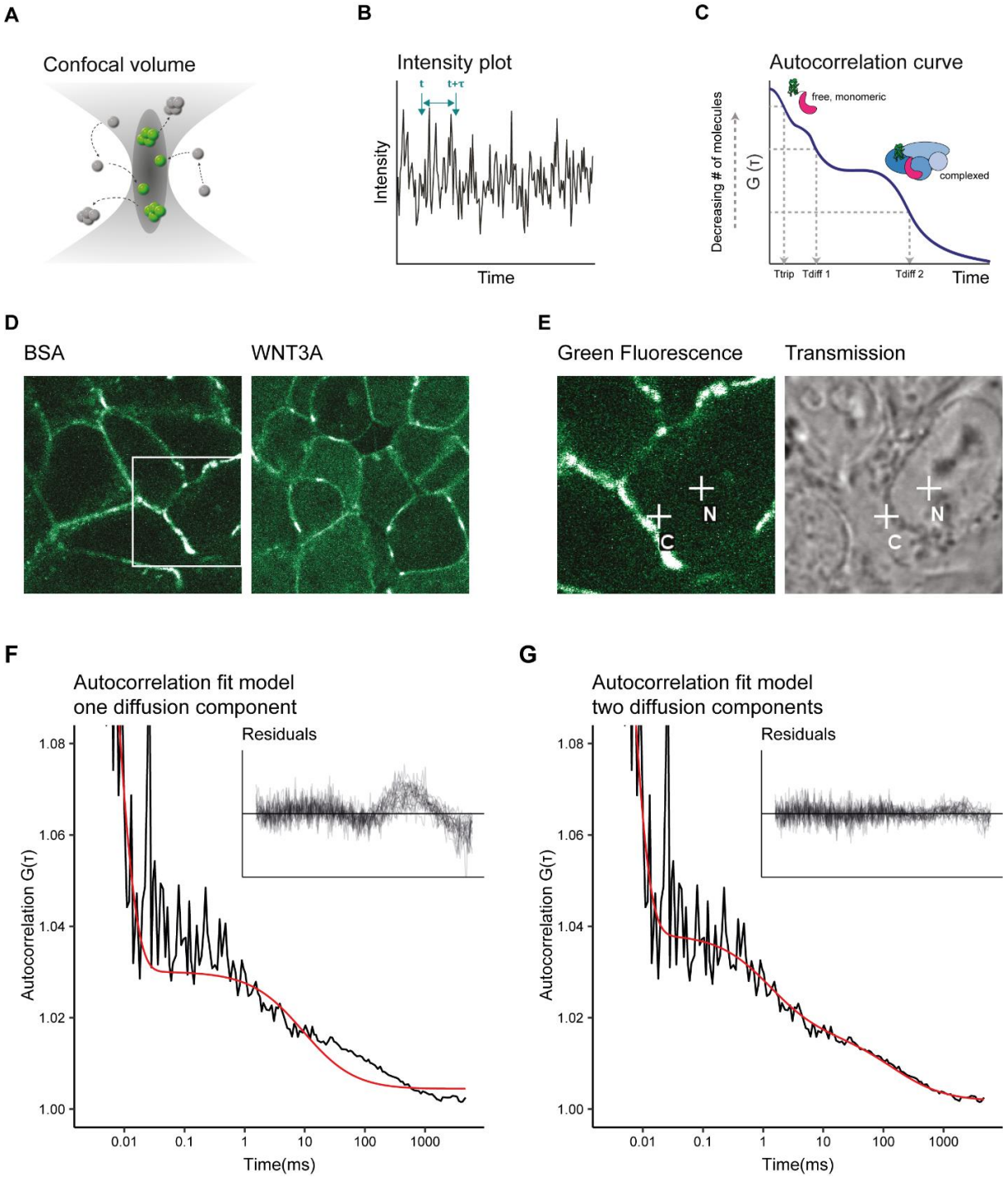

Figure 5: Two diffusion-component fit-model for SGFP2-CTNNB1 FCS measurements. A) Schematic representation of the point FCS technique, depicting the confocal volume with fluorescent particles diffusing in and out. Particles in FCS are defined by their coherent movement; therefore, a particle can be made up of monomers or multimers in isolation or complexed to unlabeled molecules. B) Schematic representation of intensity fluctuations over time as measured in the confocal volume. Fluctuations are the result of both photo-physics (e.g. blinking of the fluorophore) and diffusion. C) Graphical representation of the two diffusion-component fitting model used for our autocorrelation curves. T_{trip} describes the blinking of the SGFP2 fluorophore and the after-pulsing artefact. T_{diff1} and T_{diff2} describe the monomeric and complexed form of SGFP2-CTNNB1, respectively. Details of all fitting parameters are described in Materials and Methods. D) Representative confocal images of $HAP1^{SGFP2\text{-}CTNNB1}$ cells treated for 4 hours with BSA (left) or 100 ng/ml WNT3A (right). E) Zoom in of the white rectangle in (D), with representative locations of FCS measurement points for cytoplasm (C) and nucleus (N) indicated with white crosses in the SGFP2-CTNNB1 channel and transmission channel. F-G) Fitting of a representative autocorrelation curve with one unfixed diffusion-component (F) or a two diffusion-component model (G), where the first diffusion component was fixed to the speed of free monomeric SGFP2-CTNNB1 (14.9$\mu m^2/s$) and the second diffusion component was unfixed. The black line represents the autocorrelation curve generated from the FCS measurement, the red line represents the fitted model. The residuals after fitting of 25 individual curves are shown in the upper right corner of the graphs.

Quantification of SGFP2-CTNNB1 mobility in the nucleus

By fitting our data with this two-component diffusion model, we obtained the diffusion coefficient for the slower (i.e. complexed) CTNNB1 fraction in both the nuclear and cytoplasmic compartment. In the nucleus this second diffusion coefficient was 0.140 $\mu m^2 s^{-1}$ (median, 95%CI 0.121-0.213) in unstimulated cells and 0.178 $\mu m^2 s^{-1}$, (median, 95%CI 0.139-0.211) in cells treated with purified WNT3A (Figure 6A). This is comparable to the diffusion coefficients measured for other chromatin bound transcriptional activators (Lam et al., 2012), which could imply that this pool of SGFP2-CTNNB1 is linked to the chromatin as part of the TCF transcriptional complex (also called the "enhanceosome"). The fraction of SGFP2-CTNNB1 molecules bound to this nuclear complex increases from 0.26 (median, 95% CI 0.40-0.42) to 0.32 (median, 95%CI 0.30-0.35) upon WNT3A treatment (Figure 6B). This suggests that even in the absence of WNT3A a fraction of CTNNB1 might already be associated with the DNA and that WNT3A further stimulates the chromatin binding of CTNNB1, most likely through the TCF transcriptional complex.

Quantification of SGFP2-CTNNB1 mobility in the cytoplasm

In the cytoplasm, we determined the second diffusion coefficient of SGFP2-CTNNB1 to be 0.134 $\mu m^2 s^{-1}$ (median, 95% CI 0.124-0.196) in the absence of WNT3A stimulation (Figure 6A). This is indicative of very large complexes containing SGFP2-CTNNB1 that move with diffusion kinetics comparable to those previously observed for the 26S proteasome (C. G. Pack et al., 2014). After WNT3A treatment, the speed of the cytoplasmic complex increased 3.4-fold to 0.461 $\mu m^2 s^{-1}$ [95% CI of the median 0.367-0.573], indicating that the size of the cytoplasmic CTNNB1 complex changes when the WNT pathway is activated. However, the fraction of

CTNNB1 that is bound to a cytoplasmic complex remains largely unaltered upon WNT/CTNNB1 pathway stimulation (Figure 6B).

Determining the multimerization status of SGFP2-CTNNB1

Recent work suggests that the CTNNB1 destruction complex (also known as the "degradosome") is a large and multivalent complex, mainly as the result of AXIN and APC multimerization (reviewed in Schaefer and Peifer, 2019). The second diffusion coefficient determined by our FCS measurements, is consistent with this model. Such a large, multivalent destruction complex would be expected to have multiple CTNNB1 binding sites. To measure the multimerization status (i.e. the number of bound SGFP2-CTNNB1 molecules) within this cytoplasmic complex, we performed Number and Brightness (N&B) analysis. N&B is a fluorescence fluctuation spectroscopy technique similar to point FCS, but it makes use of image stacks acquired over time rather than individual point measurements (Digman, Dalal, Horwitz, & Gratton, 2008). By quantifying the variance in fluorescence intensity of this stack, not only the number of particles but also their brightness can be determined. Because brightness is an inherent property of a fluorophore, a change in brightness is a measure of the number of fluorophores per particle. In our case, the brightness is indicative of the number of SGFP2-CTNNB1 molecules per complex. Unfortunately, N&B does not incorporate diffusion kinetics. Therefore, we cannot differentiate between monomeric (which would have a brightness of one) and complexed CTNNB1 (which would have a brightness exceeding one if multiple CTNNB1 molecules reside in a single complex). Therefore, the measured brightness of SGFP2-CTNNB1 in our N&B analysis is the average of both fractions. We observe that the total pool of SGFP2-CTNNB1 has a brightness similar to EGFP and SGFP2 monomers in both the cytoplasm and nucleus (Figure 6C). This suggests that few, if any, of the cytoplasmic or

nuclear complexes measured by point FCS, contain multiple SGFP2-CTNNB1 molecules. If the cytoplasmic SGFP2-CTNNB1 containing complex indeed represents a large, multivalent destruction complex, this would imply that, quite unexpectedly, most CTNNB1 binding sites are unoccupied in both the absence and presence of WNT3A.

Quantification of SGFP2-CTNNB1 concentrations

FCS also allowed us to determine the absolute number of SGFP2-CTNNB1 molecules in the confocal volume (Figure 6D). After calibration of the confocal volume via reference measurements, the particle number can be converted to the concentration of endogenous SGFP2-CTNNB1 in the cell (Table 1). In the absence of WNT, the concentration of SGFP2-CTNNB1 was 202 nM (median, 95%CI 151-253) in the cytoplasm and 144 nM (median, 95%CI 111-177) in the nucleus. This is consistent with the nuclear exclusion we observed with confocal imaging (Figure 4E). We measured comparable particle numbers with N&B (Figure 6 supplement 1A).

In the presence of WNT3A, we measure a 1.1-fold increase in the total SGFP2-CTNNB1 concentration to 219 nM (median, 95%CI 173-264 nM) in the cytoplasm. This increase is smaller than expected from fluorescence intensity measurements (Figure 4C, Figure 6 supplement 1), for which we currently have no explanation. In the nucleus the concentration increases 2.1-fold to 300 nM (median, 95%CI 257-342) upon pathway activation. Nuclear concentrations of SGFP2-CTNNB1 therefore exceed cytoplasmic concentrations after WNT3A treatment, consistent with the nuclear accumulation observed with live imaging (Figure 4). Our observed concentrations of endogenous CTNNB1 in HAP1 cells are in a similar range as those previously determined by quantitative mass spectrometry in different mammalian cell lines (Kitazawa et al., 2017; Tan et al., 2012). Of note, the exact concentrations can vary

396 between cell types and may be dependent on the intricacies and assumptions of each
397 individual technique.

398 Using the fractions obtained from the FCS fitting (Figure 6B), we also determined the
399 concentration of fast (i.e. free monomeric) and slow (i.e. complexed) SGFP2-CTNNB1 (Figure
400 6E-F, Table 2). In the cytoplasm we see that the concentration of both fast and slow SGFP2-
401 CTNNB1 increases upon WNT3A treatment. This challenges the view that mainly monomeric
402 CTNNB1 accumulates, as commonly depicted (Figure 1). In the nucleus, the concentration of
403 fast moving CTNNB1 increases 2.0-fold from 95 nM (median, 95%CI 85-133) to 186 nM
404 (median, 95%CI 164-238), while slow moving CTNNB1 concentrations increase 4.4-fold from
405 23 nM (median, 95%CI 4-43) to 102 nM (median, 95%CI 67-114). The preferential increase of
406 the slow-moving fraction suggests that binding affinity of CTNNB1 to the chromatin, and
407 presumably TCF transcriptional complexes, is increased after WNT3A treatment.

408 Taken together, this is the first time that the concentrations of different functional pools of
409 endogenous CTNNB1 have been measured in living mammalian cells using functional imaging.

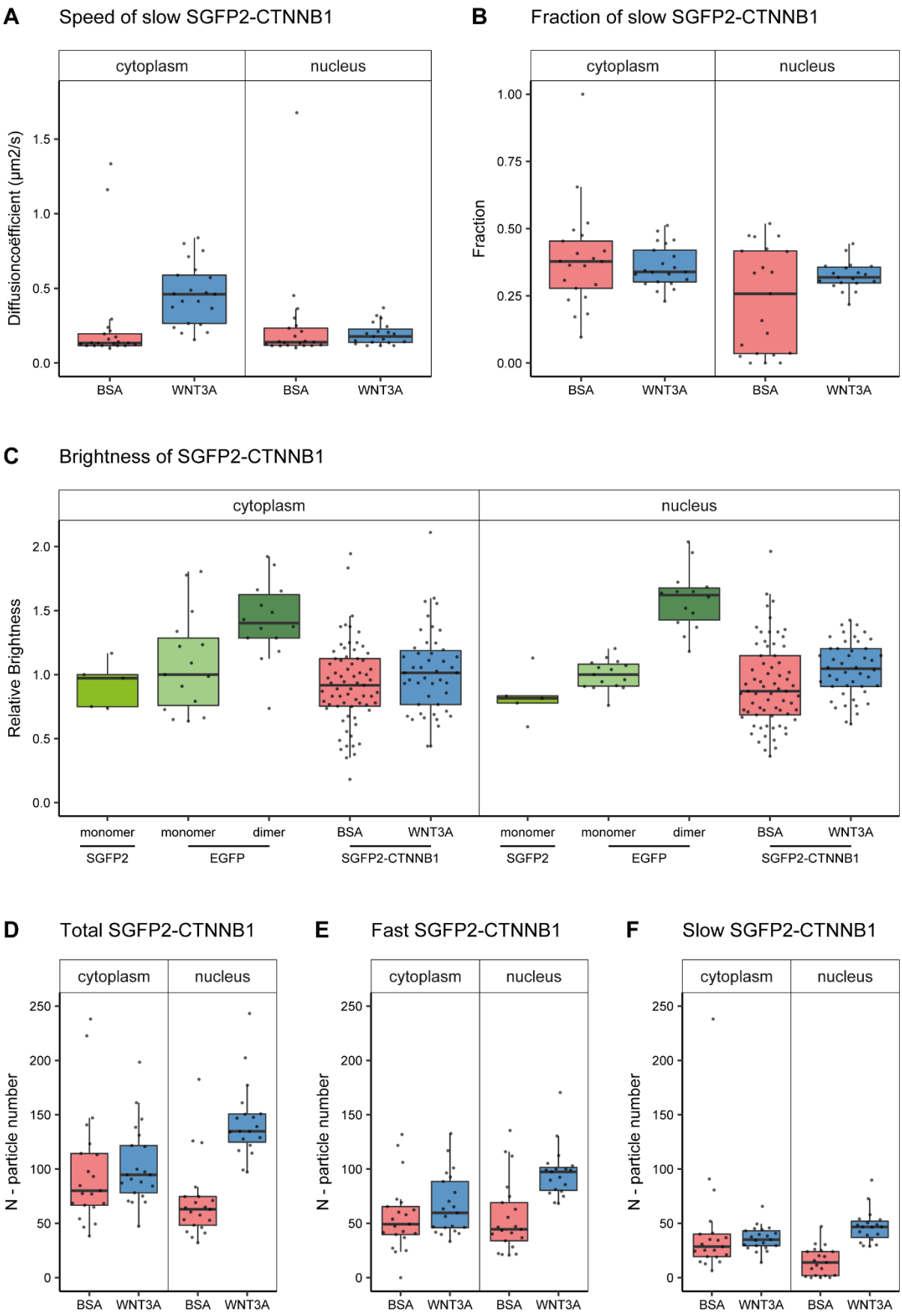

Figure 6: Mobility and abundance of SGFP2-CTNNB1 molecules in living cells after 4 hours WNT3A treatment or control. A-B) Graphs depicting the speed (A) and fraction (B) of the second diffusion component (i.e. SGFP2-CTNNB1 containing complex) measured by FCS. C) Graph depicting the molecular brightness of SGFP2-CTNNB1 in the cytoplasm and nucleus relative to controls as measured with N&B in the

same subcellular compartments. EGFP monomer was used for normalization and EGFP dimer as a control for N&B measurements. D) Graph depicting the total number of SGFP2-CTNNB1 particles (monomeric plus complexed) as measured with FCS. E) Graph depicting the number of SGFP2-CTNNB1 particles with the fast diffusion component (i.e. free monomeric). F Graph depicting the number of SGFP2-CTNNB1 containing particles with the slow diffusion component (i.e. complex associated).

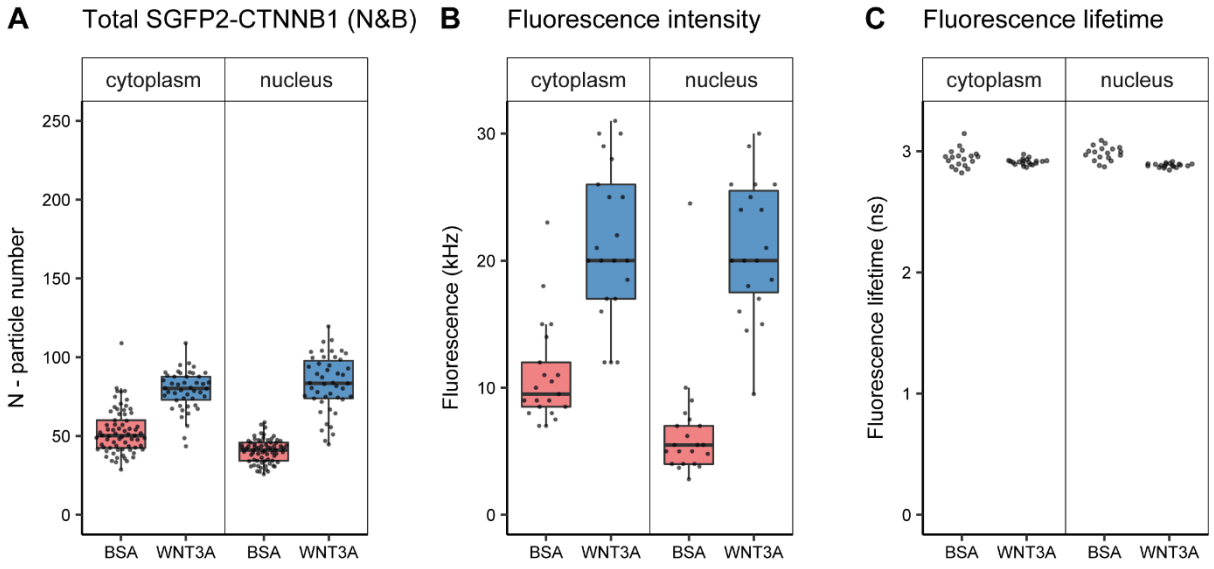

Figure 6 supplement 1 A) Graph depicting the total number of SGFP2-CTNNB1 particles as measured with N&B. B) Graph depicting the average fluorescence intensity at the start of the FCS measurement. The increase in SGFP2-CTNNB1 fluorescence in the cytoplasm (2.1-fold) exceeds the increase in the SGFP2-CTNNB1 concentration (1.1-fold, Figure 6D), but does correspond to the relative increase measured by time-lapse imaging (1.7-fold, Figure 4C). D) Graph depicting fluorescence lifetimes calculated from the FCS measurements. The Fluorescence lifetime of SGFP2-CTNNB1 is independent of the subcellular compartment and treatment. Therefore, photophysical effects are not the cause for the difference between the fold-change in fluorescence and concentrations of the FCS measurements as described in C).

Table 1: Total number of SGFP2-CTNNB1 molecules and calculated concentrations obtained with FCS

		Number of molecules		Concentration (nM)	
compartment	treatment	median	95% CI	median	95% CI
Cytoplasm	BSA	80	67-113	202	151-253
	WNT3A	95	84-121	219	173-264
Nucleus	BSA	63	53-71	144	111-177
	WNT3A	135	128-150	300	257-342

Table 2: Number and concentration of SGFP2-CTNNB1 molecules with fast or slow diffusion times obtained with FCS

		Fast SGFP2-CTNNB1				Slow SGFP2-CTNNB1			
		Number of molecules		Concentration (nM)		Number of molecules		Concentration (nM)	
compartment	treatment	median	95% CI	median	95% CI	median	95% CI	median	95% CI
Cytoplasm	BSA	49	41-65	104	70-149	29	21-37	60	42-79
	WNT3A	60	46-78	145	84-181	35	29-41	75	63-91
Nucleus	BSA	45	37-63	95	85-133	14	2-24	23	4-42
	WNT3A	97	81-100	186	164-238	47	39-51	102	67-114

A minimal computational model of WNT/CTNNB1 signaling

Quantitative measurements and physical parameters of WNT pathway components and their interactions remain limited (Kitazawa et al., 2017; Lee, Salic, Krüger, Heinrich, & Kirschner, 2003; Tan et al., 2012), especially in living cells. As we obtained measurements of different functional pools of CTNNB1, we next sought to integrate these parameters in a minimal computational model of WNT signaling to identify the critical nodes of regulation of subcellular SGFP2-CTNNB1 (Figure 7A, Table 3-4, Materials and Methods). This minimal model is based on a previous model by Kirschner and colleagues (Lee et al., 2003), and incorporates the new data obtained in our study, supplemented with parameters from literature (Lee et al., 2003; Tan et al., 2012).

Our model diverges from the model presented by Lee et al. on two major points. First, the model is simplified by omitting the details of the destruction complex cycle and the action of APC and AXIN, since our data do not provide new quantitative data on this part of the WNT/CTNNB1 signaling cascade. Second, we explicitly include shuttling of CTNNB1 between the cytoplasm and nucleus in both directions (Schmitz, Rateitschak, & Wolkenhauer, 2013; Tan, Gardiner, Hirokawa, Smith, & Burgess, 2014).

Thus, our model (Figure 7A) describes the binding of cytoplasmic CTNNB1 (‘CB’) to the destruction complex (‘DC’) leading to its phosphorylation and degradation, which releases the DC. Transport of CTNNB1 from the cytoplasm to the nucleus, allows nuclear CTNNB1 (‘NB’) to bind to TCF forming a transcriptional complex (NB-TCF). When WNT is present in the system, we describe the inactivation of the destruction complex (‘DC*’) by DVL.

Our final model faithfully recapitulates the dynamic changes that we observe with functional imaging (compare Figure 7B-F to Figure 4 and 6). Moreover, it reveals two critical regulatory

nodes in addition to the requisite inactivation of the destruction complex. The first additional node of regulation is nuclear import and export (or 'shuttling', described by k6/k7). Upon WNT stimulation, the ratio of k6/k7 needs to increase in order for the model to match the free CTNNB1 concentrations we measured by FCS (Table 4, Figure 6E). Thus, the balance shifts from nuclear export before WNT, to nuclear import after WNT. The second additional node of regulation is the association of CTNNB1 with the TCF transcriptional complex (or 'retention'), described by k9/k8. Upon WNT stimulation, the ratio of k9/k8 needs to decrease by more than a factor of 10 in order for the model to reproduce the concentrations of free and bound CTNNB1 in the nucleus as measured by FCS (Table 4, Figure 6E-F). Thus, association of CTNNB1 to the TCF transcriptional complex is favored after WNT stimulation.

In summary, our model suggests that WNT/CTNNB1 signaling is regulated at three distinct levels of the signal transduction pathway: destruction complex inactivation, nucleocytoplasmic shuttling and nuclear retention.

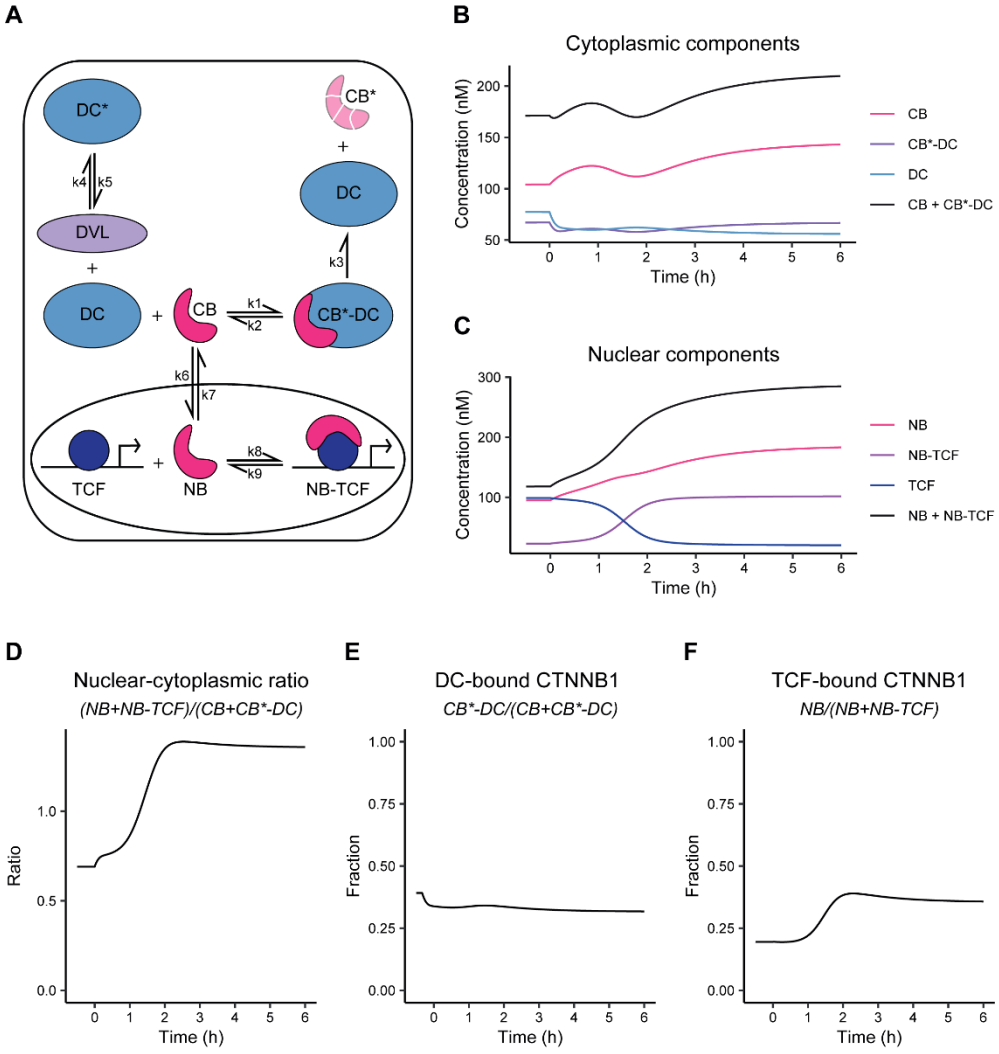

Figure 7: Computational model of WNT/CTNNB1 based on FCS for free and complexed CTNNB1 (Table 1-2). A) Schematic overview of the model. DC=destruction complex, DC*= DVL-inactivated DC, CB=cytoplasmic CTNNB1, CB*=phosphorylated CB, NB=nuclear CTNNB1, TCF=TCF/LEF transcription factors, DVL=WNT-activated DVL. The model assumes that there is no activated DVL in the absence of WNT, therefore k4/k5 do not play any role in the WNT 'OFF' equilibrium. Note that CB* is degraded and therefore plays no role in the model. B) Graph depicting the modelled concentrations of cytoplasmic components over time. The black line indicates total concentration of cytoplasmic CTNNB1, corresponding to Figure 4C. C) Graph depicting the modelled concentrations of nuclear components over time. The black line indicates total concentration of nuclear CTNNB1, corresponding to Figure 4D. D) Graph depicting the ratio of total nuclear and cytoplasmic CTNNB1 over time, corresponding to the measurements in 4E. E) Graph depicting the DC-bound CTNNB1 fraction ratio over time. F) Graph depicting the TCF-bound CTNNB1 fraction ratio over time.

Table 3: Variables Minimal Model of WNT signaling.

Model name	Variable	Compound	Values obtained from	WNT ON (nM)	WNT OFF (nM)
CB	x_1	Free cytoplasmic CTNNB1	FCS data this report	104	145
DC	x_2	Free destruction complex	Model equations	77.3	55.5
CB*-DC	x_3	DC-bound phosphorylated CTNNB1	FCS data this report*	67*	67*
DC*	x_4	Inactivated destruction complex	Model equations	0	21.6
NB	x_5	Free nuclear CTNNB1	FCS data this report	95	186
TCF	x_6	Free TCF	Model equations	99	20
NB-TCF	x_7	TCF-bound nuclear CTNNB1	FCS data this report	23	102
TCF^0	TCF^0	Total TCF	x_7 and Tan et al., 2012 - Figure 11	122	122

Under the assumption that k3 does not change, the levels of CB-DC remain equal. Since there was no significant difference between the concentration of slow SGFP2-CTNNB1 (Table 2) the average of both medians was used

Table 4: Equilibrium conditions for the Minimal Model of WNT signaling. All rates are multiplied with factor R=20, so that the equilibrium is reached at 4.5h according to Figure 4 C, D.

Rate constant		Biological process	Values based on	WNT OFF	WNT ON
b	$nMmin^{-1}$	CTNNB1 synthesis	v_{12} from Lee	0.423	0.423
$\frac{k_2}{k_1}$	nM	Binding to and phosphorylation by the destruction complex of cytoplasmic CTNNB1	K_8 from Lee	120	120
k_3	min^{-1}	Dissociation and degradation of phosphorylated CTNNB1 from the destruction complex	Deduced from b and x_3	0.0063	0.0063
$\frac{k_5}{k_4}$	nM	Inactivation of the destruction complex by activated DVL	Fitted to x_1 and x_7	N.A.	2.56
$\frac{k_6}{k_7}$		Ratio between nuclear import and export of CTNNB1	Deduced from x_1 and x_5	0.913	1.28
$\frac{k_9}{k_8}$	nM	Dissociation of nuclear CTNNB1 from TCF	Deduced from x_5, TCF^0, x_7	409	36.5

Discussion

WNT signaling is a critical pathway for tissue development and homeostasis. Although most core players and many of their molecular interaction mechanisms have been uncovered, dynamic spatiotemporal information at the endogenous level and with subcellular resolution is very limited. As both genome editing approaches and quantitative live-cell microscopy have advanced further, the goal of studying WNT/CTNNB1 signaling at endogenous expression levels in living cells now is within reach. Maintaining endogenous expression levels is important, as overexpression may lead to altered stoichiometry of signaling components, as well as changes in subcellular localization (T. J. Gibson et al., 2013; Mahen et al., 2014). Indeed, it has been shown that exogenously expressed CTNNB1 is less signaling competent, probably due to its post-translational modification status (Hendriksen et al., 2008). Here we generated and characterized clonal HAP1$^{SGFP2\text{-}CTNNB1}$ knock-in cell lines to study the dynamic behavior and subcellular complex state of endogenous CTNNB1 in individual living human cells in the presence and the absence of WNT pathway activation (Figure 2-3).

Using live-cell microscopy and automated cell segmentation we observe that endogenous CTNNB1 only increases 1.7-fold in the cytoplasm and 3.0-fold in the nucleus after WNT3A treatment, which is consistent with the literature (Jacobsen et al., 2016; Kafri et al., 2016; Massey et al., 2019). Our data show a faster increase of endogenous CTNNB1 upon GSK3 inactivation or WNT stimulation than two recent studies that used chromobody labeling (Keller et al., 2018; Traenkle et al., 2015). This could be a cell type specific difference, but might also be related to the background expression levels of unbound chromobodies that could mask subtle and early changes in endogenous protein levels. In addition, we show that the response to WNT3A stimulation and even to global GSK3 inhibition is heterogeneous (Figure 4A, Figure 4 supplement 2A-B). There are indications that cell cycle, adhesion status

and mechano-signaling are important in determining the WNT response (Benham-Pyle, Pruitt, & Nelson, 2015; Benham-Pyle, Sim, Hart, Pruitt, & Nelson, 2016; Gayrard, Bernaudin, Déjardin, Seiler, & Borghi, 2018; Howard, Deroo, Fujita, & Itasaki, 2011; Kafri et al., 2016; Olmeda, Castel, Vilaró, & Cano, 2003; van Leeuwen, Byrne, Jensen, & King, 2007). Although, it will be interesting to use live-cell imaging to further uncover the roles of these factors in determining the cell-to-cell variability in WNT responsiveness in the future, here we focus on novel regulatory aspects of CTNNB1 in the cytoplasm and nucleus.

Cytoplasmic regulation of CTNNB1

Using FCS, we show for the first time that CTNNB1 resides in slow moving complexes in the cytoplasm of living mammalian cells (Figure 5-6). The main known cytoplasmic complex containing CTNNB1 is the destruction complex. The combined weight of the individual destruction complex components (AXIN, APC, CSNK1 and GSK3) would be expected to result in a much higher mobility than the cytoplasmic CTNNB1-containing complex we observed. Currently, evidence is growing that the destruction complex forms phase separated aggregates (also termed biomolecular condensates) (reviewed in Schaefer and Peifer, 2019). Oligomerization of AXIN and APC underlies the formation of these aggregates, and this in turn appears to be required for efficient degradation of CTNNB1 (Fiedler, Mendoza-Topaz, Rutherford, Mieszczanek, & Bienz, 2011; Kunttas-Tatli, Roberts, & McCartney, 2014; Pronobis, Deuitch, Posham, Mimori-Kiyosue, & Peifer, 2017; Spink, Polakis, & Weis, 2000). There is some evidence that these aggregates form at (near) endogenous levels (Fagotto et al., 1999; Faux et al., 2008; Mendoza-Topaz, Mieszczanek, & Bienz, 2011; Pronobis, Rusan, & Peifer, 2015; Schaefer et al., 2018; Thorvaldsen et al., 2015), but it is still an open question what the exact composition and size of the destruction complex is in a physiological context. It should

be noted that our imaging does not visualize such aggregates (Figure 4A). Nevertheless, the diffusion coefficients we observed for the cytoplasmic CTNNB1 complex are compatible with a large complex. Interestingly, our N&B data indicate that few, if any, complexes exist that contain multiple SGFP2-CTNNB1 molecules, which would logically be expected for a large oligomerized destruction complex with multiple CTNNB1 binding sites.

Alternative explanations for the slow diffusion speed of the cytoplasmic CTNNB1 complex include a monovalent destruction complex in association with (parts of) the proteasome machinery (Li et al., 2012; Lui et al., 2011; Schaefer et al., 2020) or anchoring of either CTNNB1 itself or any of its interaction partners to the cytoskeleton (reviewed in Bryja et al., 2017; Fagotto, 2013). Therefore, additional data on the localization and mobility of other endogenously tagged WNT pathway components are required to determine the exact identity of the slow-diffusing, cytoplasmic CTNNB1 complex.

Of note, our data clearly show that a substantial fraction of CTNNB1 in the cytoplasm remains bound upon pathway stimulation (Figure 6B). Additionally, we show that this complex has an increased mobility compared to control treated cells (Figure 6A). Therefore, while the diffusion coefficient is still very low (indicating a very large complex), this implies it is a different complex than that observed in the absence of WNT stimulation. The current literature suggests that the destruction complex is sequestered to the FZD-LRP receptor complex upon WNT pathway stimulation. Several models exist for how the membrane sequestration inhibits CTNNB1 degradation, including LRP mediated GSK3 inhibition (Stamos, Chu, Enos, Shah, & Weis, 2014), sequestration of GSK3 in multi vesicular bodies (Taelman et al., 2010), (partial) dissociation of the destruction complex (X. Liu, Rubin, & Kimmel, 2005; Tran & Polakis, 2012), and saturation of CTNNB1 within an intact destruction complex (Li et

al., 2012). None of these models include a remaining cytoplasmic CTNNB1 complex in the presence of WNT ligands, but our data suggest that such a complex must exist.

Nuclear regulation of CTNNB1

The key function of CTNNB1 downstream of WNT is to regulate transcription of TCF/LEF target genes (Doumpas et al., 2019; Schuijers, Mokry, Hatzis, Cuppen, & Clevers, 2014). Proteomic analyses have shown that the WNT-responsive transcriptional complex consists of CTNNB1, TCF/LEF, PYGO and BCL9 and several other large proteins (Fiedler et al., 2015; van Tienen et al., 2017). Using FCS we showed that CTNNB1 resides in a nuclear complex with a diffusion coefficient that is compatible with such a DNA-bound transcriptional complex (Figure 6A) (Lam et al., 2012). Upon pathway activation we see an increase in the fraction and absolute levels of this slow-diffusing nuclear CTNNB1 complex, consistent with increased CTNNB1 binding to its target sites (Figure 6B, F). The concentration increases to a 102 nM, which corresponds to something in the order of 20.000 bound CTNNB1 molecules in one nucleus, assuming a small nuclear volume of 0.36 pL (Tan et al., 2012). Published CHIPseq studies report many CTNNB1 DNA binding sites, ranging from several hundred to several thousand sites in mammalian cells (Cantù et al., 2018; Doumpas et al., 2019; Schuijers et al., 2014). It is therefore conceivable that at least some of the slow-diffusing CTNNB1 particles we measure represent CTNNB1 that is associated with DNA bound TCF transcriptional complexes.

Although CTNNB1 is known to associate with TCF/LEF factors in response to WNT/CTNNB1 signaling to drive transcription (Franz, Shlyueva, Brunner, Stark, & Basler, 2017; Schuijers et al., 2014), we also detect low levels of nuclear CTNNB1 complex in the absence of a WNT stimulus (Figure 6B,F). The diffusion coefficient of the nuclear CTNNB1 complex does not change upon the addition of WNT3A, suggesting that some CTNNB1 is already associated with

578 the DNA even in the absence of a WNT stimulus. Whether the nuclear CTNNB1 complex,
579 either in the absence or presence of WNT, truly represents TCF/LEF associated CTNNB1
580 remains to be determined. At this point, we cannot exclude the contribution to TCF/LEF
581 independent DNA binding (Armstrong, Fagotto, Prothmann, & Rupp, 2012; Essers et al., 2005;
582 Kormish, Sinner, & Zorn, 2010), or anomalous subdiffusion in the nucleus, either due to
583 physical obstruction , transient DNA-binding events protein or protein complex formation
584 (Dross et al., 2009; Kaur et al., 2013; Wachsmuth, Waldeck, & Langowski, 2000).

585 Regulation of CTNNB1 nuclear accumulation

586 In HAP1 cells, endogenous CTNNB1 is excluded from the nucleus in the absence of WNT. Our
587 live imaging data reveal an immediate and preferential increase in nuclear CTNNB1 upon
588 WNT3A stimulation, until an equilibrium is reached between the cytoplasmic and nuclear
589 levels (Figure 4E, Figure 6D). This has previously been observed in HEK293 cells stably
590 overexpressing low levels of YFP-CTNNB1 (Kafri et al., 2016). Indeed, our computational
591 model can explain this preferential increase in nuclear CTNNB1 by a shift in the balance of
592 nuclear translocation from nuclear export to nuclear import after the addition of WNT3A
593 (Figure 7). This suggests that WNT signaling not only regulates the absolute levels of CTNNB1
594 through destruction complex inactivation, but also actively changes its subcellular
595 distribution.

596 Intriguingly, CTNNB1 does not contain nuclear import or export signals and can translocate
597 independently of classical importin and exporter pathways (Fagotto, Glück, & Gumbiner,
598 1998; Wiechens & Fagotto, 2001; Yokoya, Imamoto, Tachibana, & Yoneda, 1999). Hence, the
599 molecular mechanism of CTNNB1 subcellular distribution remains incompletely understood.
600 Evidence from Fluorescence Recovery After Photobleaching (FRAP) studies suggest that the

increase in nuclear CTNNB1 is due to changes in binding to its interaction partners in the cytoplasm and nucleus (retention) rather than active changes in nuclear import and export rates (shuttling) (Jamieson, Sharma, & Henderson, 2011; Krieghoff, Behrens, & Mayr, 2006). We argue that the two are not mutually exclusive, as our experimental data and computational model suggest that WNT regulates both nucleocytoplasmic shuttling and nuclear retention of CTNNB1. Indeed, we see an increase of nuclear CTNNB1 complexes in the nucleus (Figure 6B, F) and the dissociation of CTNNB1 from TCF is reduced over 10-fold in WNT signaling conditions in our computational model (Table 4). This could be achieved through posttranslational modification and conformational changes in CTNNB1 as proposed by others (Gottardi & Gumbiner, 2004; Sayat, Leber, Grubac, Wiltshire, & Persad, 2008; Wu et al., 2008).

Challenges and opportunities for fluorescence fluctuation spectroscopy techniques

Using fluorescence fluctuation spectroscopy techniques (FCS and N&B) we have quantified endogenous CTNNB1 concentrations and complexes in living cells for the first time. This has yielded novel insights into the CTNNB1 complex state and new parameters for computational modelling. As with any technique, there are several limitations of point-FCS that we should consider.

First, we are limited by the assumptions we make in the FCS fitting model used. Although obvious mistakes in assumptions immediately become clear due to bad fitting results and can therefore be excluded, not every wrong assumption will stand out accordingly. Our data clearly shows that assuming only one diffusion speed for CTNNB1 in cells would be incorrect (Figure 5). However, whether we measure a single distinct large complex with the second diffusion speed, or rather an average of multiple different CTNNB1 containing complexes

cannot be determined in our current set-up. In addition, we assume that CTNNB1 is present as a free-floating monomer (as fixed for our first component), based on previous observations (Gottardi & Gumbiner, 2004; Maher et al., 2010). However, at least one report suggests that CTNNB1 is not present as a monomer but rather in small cytoplasmic complexes of ~200 kDa (Gerlach, Emmink, Nojima, Kranenburg, & Maurice, 2014). As diffusion speed is relatively insensitive to differences in size (e.g. an 8-fold increase in protein mass is expected to result in only a 2-fold reduction of the diffusion coefficient for a spherical particle), it is possible that we do not measure truly free-floating CTNNB1, but rather smaller complexes.

Secondly, point FCS gives an indication of the size of the cytoplasmic and nuclear complexes we observe. However, it cannot provide conclusive evidence on their composition. An exciting possibility would be to label additional components presumed to be present in the CTNNB1-containing complexes at the endogenous level to uncover the precise composition and stoichiometry of protein complexes involved in WNT signaling. For instance Fluorescence Cross Correlation Spectroscopy (FCCS) could be employed to test if two proteins reside within the same complex (Elson, 2011; Hink, 2014; Macháň & Wohland, 2014). A combination of such functional imaging techniques, biochemical and proteomic approaches, together with specific perturbations and mutant versions of candidate proteins can be employed to further our understanding of the dynamic composition of endogenous CTNNB1 complexes, as well as to help us resolve how WNT signaling alters nucleocytoplasmic shuttling of CTNNB1 and specifically induces nuclear retention of CTNNB1.

Summary and outlook

In conclusion, we generated a functional fluorescent endogenous CTNNB1 fusion using CRISPR/Cas9-mediated genome editing. Using live imaging we show a preferential increase in

nuclear accumulation of CTNNB1 upon WNT pathway stimulation. Furthermore, state-of-the-art, quantitative microscopy revealed changes in the abundance and identity of nuclear and cytoplasmic CTNNB1 complexes upon WNT pathway activation. Combining our experimental data with computational modeling of WNT/CTNNB1 signaling reveals that WNT regulates the dynamic distribution of CTNNB1 across different functional pools not only by modulating the destruction complex, but also by actively changing nucleocytoplasmic shuttling and nuclear retention.

Quantitative functional analyses of proteins at endogenous levels will help us to further understand the mechanisms of WNT/CTNNB1 signaling and other cellular signal transduction pathways. As both genome editing and live cell imaging techniques continue to improve, additional possibilities will open up to address longstanding questions in cellular signaling in a physiological context with high spatial and temporal resolution. New opportunities and challenges await as these investigations extend to 3D organoid cultures, developing embryos and living organisms.

Material and Methods

DNA Constructs

The following constructs were used: pSpCas9(BB)-2A-Puro (PX459) V2.0 ((Ran et al., 2013), a kind gift from Feng Zhang, available from Addgene, plasmid #62988), MegaTopflash ((Hu et al., 2007), a kind gift from Dr. Christophe Fuerer and Dr. Roel Nusse, Stanford University), CMV Renilla (E2261,Promega, Madison, WI), pSGFP2-C1 ((G.-J. Kremers et al., 2007), a kind gift from Dorus Gadella, available from Addgene, plasmid #22881), pmScarlet-i_C1 (Bindels et al., 2017), a kind gift from Dorus Gadella, available from Addgene, plasmid # 85044), pSYFP2-C1 ((G. J. Kremers et al., 2006),a kind gift from Dorus Gadella, available from Addgene, plasmid #22878), mTurquoise2-C1 ((Goedhart et al., 2012), a kind gift from Dorus Gadella, available from Addgene, plasmid # 54842), pEGFP (Clontech, Mountain View, CA), $pEGFP_2$ ((C. Pack, Saito, Tamura, & Kinjo, 2006), a kind gift from Masataka Kinjo) and pBluescript II KS(+) (Stratagene, La Jolla, CA).

The gRNA targeting the start codon in exon2 of human *CTNNB1* was designed using the MIT webtool (crispr.mit.edu) and cloned into pX459. Oligos RVA567 and RVA568 (Table 5) encoding the gRNA were annealed, and ligated into BbsI-digested pX459 plasmid as previously described (Ran et al., 2013) to obtain pX459-CTNNB1-ATG.

The repair plasmid for SGFP2-CTNNB1 (pRepair-SGFP2-CTNNB1) was cloned using Gibson cloning (D. G. Gibson et al., 2009). First, a repair plasmid including the Kozak sequence from the pSGFP2-C1 plasmid was generated (pRepair-Kozak-SGFP2 -CTNNB1). For this, 5' and 3' homology arms were PCR amplified from genomic HEK293A DNA with primers RVA618 and RVA581 (5' arm) or RVA619 and RVA584 (3' arm). SGFP2 was amplified with Gibson cloning from pSGFP2-C1 with primers RVA582 and RVA583 and the backbone was amplified from SacI

digested pBlueScript KS(+) with primers RVA622 and RVA623. The final repair construct (pRepair-SGFP2-CTNNB1) contains the endogenous *CTNNB1* Kozak sequence before the SGFP2 ATG. To obtain (pRepair-SGFP2-CTNNB1), the backbone and homology regions were amplified from pRepair-SGFP2-Kozak-CTNNB1 with primers RVA1616 and RVA1619 and an SGFP2 without the Kozak sequence was amplified from pSGFP2-C1 with primers RVA1617 and RVA1618. To generate color variants of the repair plasmid SYFP2, mScarlet-i and mTurquoise2 were also amplified from their respective C1 vectors with primers RVA 1617 and RVA 1618. PCR products were purified and assembled with a Gibson assembly master mix with a 1:3 (vector:insert) molar ratio. Gibson assembly master mix was either purchased (E2611S, NEB) or homemade (final concentrations: 1x ISO buffer (100mM Tris-HCL pH 7.5, 10mM MgCl2, 0.2M dNTPs (R0181, Thermo Scientific), 10mM DTT (10792782, Fisher), 5% PEG-8000 (1546605, Sigma-Aldrich, St Louis, MO), 1mM NAD+ (B9007S, NEB)), 0.004 U/µl T5 exonuclease (M0363S, NEB), 0.5 U/µl Phusion DNA Polymerase (F-530L, Thermo Scientific) and 4 U/µl Taq DNA ligase (M0208S, NEB)).

The following plasmids are available from Addgene: pX459-CTNNB1-ATG (#153429), pRepair-SGFP2-CTNNB1 (#153430), pRepair-mScI-CTNNB1 (#153431), pRepair-SYFP2-CTNNB1 (#153432), pRepair-mTq2-CTNNB1 (#153433)).

Primers used

Table 5: primers/oligonucleotides used in this study

RVA24	CAAGTTTGTTGTAGGATATGCCC
RVA25	CGATGTCAATAGGACTCCAGA
RVA124	AGTGTGAGGTCCACGGAAA
RVA125	CCGTCATGGACATGGAAT
RVA567	CACCGTGAGTAGCCATTGTCCACGC
RVA568	AAACGCGTGGACAATGGCTACTCAC
RVA581	tgctcaccatggtggGATTTTCAAAACAGTTGTATGGTATACTTC
RVA582	actgttttgaaaatcCCACCATGGTGAGCAAGGGC

RVA583	agtagccattgtccaCTTGTACAGCTCGTCCATGCCG
RVA584	gacgagctgtacaagTGGACAATGGCTACTCAAGGTTTG
RVA618	atacgactcactatagggcgaattggagctGATGCAGTTTTTTTCAATATTGC
RVA619	ttctagagcggccgccaccgcggtggagctCTCTCTTTTCTTCACCACAACATTTTATTTAAAC
RVA622	AAGAGAGAGCTCCACCGCGGTGGCGGCCG
RVA623	TGCATCAGCTCCAATTCGCCCTATAGTGAGTCG
RVA1616	tgtccacgctgGATTTTCAAAACAGTTGTATGG
RVA1617	atacaactgttttgaaaatccagcgtggacaATGGTGAGCAAGGGCGAG
RVA1618	cacaaaccttgagtagccatCTTGTACAGCTCGTCCATGC
RVA1619	ATGGCTACTCAAGGTTTGTGTCATTAAATC

Cell Culture, Treatment and Transfection

HAP1 cells (a kind gift from Thijn Brummelkamp, NKI) were maintained in full medium (colorless IMDM (21056023, Gibco, Thermo Fisher Scientific, Waltham, MA) supplemented with 10% FBS (10270106, Gibco) and 1X Glutamax (35050061, Gibco)) under 5% CO2 at 37°C in humidifying conditions and passaged every 2-3 days using 0.25% Trypsin-EDTA (25200056, Gibco). Cells were routinely tested for mycoplasma. We verified the haploid identity of the parental HAP1WT by karyotyping of metaphase spreads. To maintain a haploid population, cells were resorted frequently (see below) and experiments were performed with low passage number cells.

Where indicated, cells were treated with CHIR99021 (6mM stock solution in DMSO) (1677-5, Biovision, Milpitas, CA) or Recombinant Mouse Wnt-3a (10µg/ml stock solution in 0.1% BSA in PBS) (1324-WN-002, R&D systems, Bio-Techne, Minneapolis, MN) with DMSO and 0.1% BSA in PBS as vehicle controls, respectively.

Cells were transfected using Turbofect (R0531, ThermoFisher, Thermo Fisher Scientific, Waltham, MA), X-tremeGene HP (6366546001, Roche, Basel, Switzerland) or Lipofectamine

720 3000 (Invitrogen, Thermo Fisher Scientific, Waltham, MA) in Opti-MEM (Gibco) according to
721 the manufacturer's instructions.

722 HAP1$^{SGFP2\text{-}CTNNB1}$ generation

723 800.000 HAP1 cells/well were plated on 6-well plates. The following day, cells were
724 transfected with Turbofect and 2000 ng DNA. pX459-CTNNB1-ATG and pRepair-SGFP2-
725 CTNNB1 were transfected in a 2:1, 1:1 or 1:2 ratio. pSGFP2-C1, pX459 or pX459-CTNNB1-ATG
726 were used as controls. From 24 to 48 hours after transfection cells were selected with 0.75
727 µg/ml puromycin (A1113803, Gibco). Next, cells were expanded and passaged as needed until
728 FACS sorting at day 9. For FACS analysis and sorting cells were washed, trypsinized,
729 resuspended with full medium and spun down at 1000 rpm for 4 minutes. For sorting, cells
730 were stained with 1 µg/ml Dapi (D1306, Invitrogen) in HF (2 % FBS in HBSS (14175053, Gibco)),
731 washed with HF and resuspended in HF. To determine the haploid population, a separate
732 sample of cells was stained with 5 µM Vybrant® DyeCycleTM Violet Stain (V35003, Invitrogen)
733 in full medium for 30 minutes and kept in vibrant containing medium. Cells were filtered with
734 a 70 µm filter and then used for FACS sorting and analysis on a FACSARIA3 (BD, Franklin Lanes,
735 NJ). Vybrant-stained cells were analyzed at 37° and used to set a size gate only containing
736 haploid cells. Dapi-stained cells were single cell sorted at 4°C into 96-well plates, that were
737 previously coated overnight with 0.1 % gelatin (G9391, Sigma-Aldrich) in MQ and contained
738 full medium supplemented with 1 % penicillin/streptomycin (15140122, Gibco) and 0.025 M
739 HEPES (H3375 Sigma-Aldrich, 1 M stock solution, pH 7.4, filter sterilized). The 3 independent
740 clones used in this study were obtained from separate transfections of the same parental cell
741 line. Resorting of the cell lines was performed with the same FACS procedure, with collection
742 of cells in 15 mL tubes containing full medium with 1 % penicillin and 0.025 M HEPES.

FACS data were analyzed and visualized with FlowJo™.

qPCR

For qPCR analysis, 100.000 HAP1 cells per well were seeded on a 24-well plate. After 48 hours, cells were treated with indicated concentrations of CHIR99021. Cells were harvested 24 hours after treatment. RNA was isolated with Trizol (15596018, Invitrogen) according to the manufacturer's instructions. cDNA was synthesized using SuperScriptIV (18090010, Invitrogen) according to the manufacturer's instructions. qPCR was performed with SyberGreen (10710004, Invitrogen). The endogenous WNT target gene *AXIN2* was amplified using primers RVA124 and RVA125, and HPRT housekeeping control was amplified using primers RVA24 and RVA25. Relative expression levels of *AXIN2* were calculated using the comparative Delta-Ct method (Livak & Schmittgen, 2001; Schmittgen & Livak, 2008). Briefly, *AXIN2* expression was normalized for *HPRT* expression and then the relative fold-change to a WT DMSO sample was calculated for all clones and conditions.

Luciferase Assay

For luciferase assays, 100.000 cells per well were seeded on a 24-well plate. Cells were transfected with 1µl X-tremeGene HP and 400 ng MegaTopflash reporter and 100 ng CMV-Renilla or 500 ng SGFP2-C1 as a negative control 24 hours later. Cells were treated with the indicated concentration of CHIR99021 24 hours after transfection and after another 24 hours medium was removed and the cells were harvested with 50 µl Passive Lysis Buffer (E1941, Promega). Luciferase activity was measured on a GloMax Navigator (Promega) using 10µl lysate in a black OptiPlate 96-well plate (6005279, Perkin Elmer, Waltham, MA) and 50 µL homemade firefly and luciferase reagents (according to (Fuerer, Nostro, & Constam, 2014; Hampf & Gossen, 2006)). Renilla and Luciferase luminescence values were corrected by

766 subtracting the background measured in the SGFP2-transfected control. MegaTopflash
767 activity was calculated as the ratio of corrected Firefly and Renilla luminescence and
768 normalized to the relative DMSO control.

769 Western Blot

770 The remaining lysates of the luciferase assay were cleared by centrifugation for 10 minutes at
771 12.000 g at 4°C. Western blot analysis was performed and quantified as previously described
772 (Jacobsen et al., 2016). Antibodies were used with the following dilutions, 1:1000 Non-
773 phosphorylated (Active) β-catenin clone D13A1 (8814S, Cell Signaling, Danvers, MA), 1:2000
774 total β-catenin clone 14 (610153, BD), 1:1000 α-Tubulin clone DM1A (T9026, Sigma-Aldrich),
775 1:1000 GFP polyclonal (A-6455, Invitrogen), 1:20.000 IRDye 680LT Goat anti-Rabbit IgG (926-
776 68021, LI-COR, Lincoln, NE), 1:20.000 IRDye 800CW Donkey anti-Mouse IgG (926–32212, LI-
777 COR).

778 Time-lapse imaging

779 The day before imaging, 88.000 cells/well were seeded on an 8 well chamber slide with glass
780 bottom (80827-90, Ibidi, Gräfelfing, Germany). HAP1$^{SGFP2\text{-}CTNNB1}$ clone 2 was used for the main
781 Figure 4, all 3 clones were used for Figure 4 supplement 1. Approximately 6 hours before
782 imaging, medium was replaced with full medium supplemented with 1%
783 penicillin/streptomycin, 0.025M HEPES and 500nM SiR-DNA (SC007, Spirochrome, Stein am
784 Rhein, Switzerland). Time lapse experiments were performed on an SP8 confocal microscope
785 (Leica Microsystems, Wetzlar, Germany) at 37°C with a HC PL APO CS2 63x/1.40 oil objective
786 (15506350, Leica), 488 and 633 lasers, appropriate AOBS settings, using HyD detectors for
787 fluorescent signal with a 496-555 for SGFP2-CTNNB1 and 643-764 bandpass for SiR-DNA, and
788 a transmission PMT. Using multi-position acquisition, up to 24 images were captured every 5

minutes. Focus was maintained using AFC autofocus control on demand for every time point and position. Automated cell segmentation and intensity quantification was performed using a custom CellProfiler™ pipeline (made available at https://osf.io/6pmwf/). Intensities were normalized per position to the average intensity in the cellular compartment (nucleus or cytoplasm) for that position before the addition of the compounds. The nuclear cytoplasmic ratio was calculated by dividing the raw nuclear intensity by the raw cytoplasmic intensity. Movies and still images were extracted with FIJI/ImageJ.

FCS and N&B cell preparation and general settings

Two days before FCS and N&B experiments, 44.000 cells/well ($HAP1^{WT}$ or $HAP1^{SGFP2\text{-}CTNNB1}$ clone 2) were seeded on an 8-well chamber slide with a glass bottom (80827-90, Ibidi). The day before measuring, $HAP1^{WT}$ cells were transfected with ~5 ng pSGFP2-C1, EGFP or EGFP dimer and ~200 ng pBlueScript KS(+) per well with X-tremeGene HP or Lipofectamine 3000. Lipofectamine 3000 yielded better transfection efficiency.

FCS and N&B measurements were performed on an Olympus FV-1000 equipped with SepiaII and PicoHarp 300 modules (Picoquant, Berlin, Germany) at room temperature. An Olympus 60x water immersed UPLS Apochromat (N.A. 1.2) objective was used for FCS acquisition and Figure 3 supplement 1E, and an Olympus 60x silicon immersed UPLS Apochromat (N.A. 1.4) objective was used for N&B measurements. Green fluorophores were excited with a 488 nm diode laser (Picoquant) pulsing at 20 MHz and detected through a 405/480-488/560/635 nm dichroic mirror (Chroma, Bellows Falls, VT) and 525df45 nm bandpass filter (Semrock, Rochester, NY) with an Avalanche Photodiode (APD) (MPD, Bolzano, Italy). For, figure 3 supplement 1E and for FCS and N&B reference images the same laser and dichroic were used,

but the signal was detected through a 505-540 bandpass filter with an internal PMT of the FV-1000 Olympus microscope.

FCS data acquisition and analysis

For FCS measurements, a confocal image of HAP1$^{SGFP2\text{-}CTNNB1}$ was recorded. In this reference image, a single pixel was set as region of interest (ROI), based on its localization in the cytoplasm or nucleus as judged by the transmission image. In this ROI, the fluorescence intensity was measured over time using an APD, for typically 120 seconds.

FCS measurements were analyzed in FFS Dataprocessor version 2.3 (SSTC, Minsk, Belarus). The autocorrelation curve ($G(\tau)$) was calculated from the measured intensity (I) according to equation 1. Intensity traces with significant photobleaching, cell movement or focal drift were excluded from further analysis. From other traces a portion of the trace with minimal (less than 10%) intensity drift or bleaching was selected to generate autocorrelation curve (AC).

$$G(\tau) = 1 + \frac{< \delta I(t) * \delta I(t+\tau) >}{< I >^2} \qquad \text{Eq. 1}$$

The resulting AC was fitted with a Triplet-state-diffusion model, described in equation 2. G_∞ accounts for offset in the AC caused by intensity drift. N is the average of the number of particles that reside in the confocal volume. F_{trip} and τ_{trip} describe the fraction of molecules in the dark state and the relaxation of this dark state respectively. Of note, in this case, F_{trip} and τ_{trip} account both for blinking of the fluorescent molecules and for the afterpulsing artefact of the APD. $\tau_{diff,i}$ describes the diffusion rate of the fluorescent molecules with the corresponding fraction, F_i. This diffusion time depends on the structural parameter (sp), which is defined as the ratio of the axial (ω_z) over the radial axis (ω_{xy}) of the observation volume.

$$G(\tau) = G_\infty + \frac{1}{< N >} * \frac{F_{trip}}{1 - F_{trip}} e^{\frac{-\tau}{\tau_{trip}}} * \sum_j \frac{F_i}{\left(1 + \frac{\tau}{\tau_{diff,i}}\right)\sqrt{1 + \frac{\tau}{\tau_{diff,i} * sp^2}}} \quad \text{Eq. 2}$$

The apparent particle numbers (N_{apa}) for SGFP2-CTNNB1 were corrected for autofluorescence and bleaching (equation 3). The autofluorescence ($I_{autofluorescence}$) of HAP1 cells in the nucleus and cytoplasm was measured in untransfected HAP1 cells using the same settings as for FCS measurements. The correction for moderate bleaching is based on the intensity of the selected portion of the intensity trace for AC calculation (I_{ana}) and the intensity at the start of the measurement (I_{start}).

The size and shape of the observation volume was calibrated daily by measuring Alexa Fluor™ 488 NHS Ester (A20000, Molecular probes, Thermo Scientific, stock dilution in MQ) in PBS in a black glass-bottom cell imaging plate with 96 wells (0030741030, Eppendorf, Hamburg, Germany). From the FCS measurements of Alexa488, the τ_{diff} and sp were determined by fitting with a single diffusion and blinking component. The diffusion coefficient (D) of Alexa488 in aqueous solutions at 22.5 °C is 435 $\mu m^2 s^{-1}$ (Petrášek & Schwille, 2008). From these parameters, the axial diameter can be determined with equation 4 and the volume can be approximated by a cylinder (equation 5). This allows for transformation of particle numbers to concentrations (equation 5) and diffusion times to diffusion coefficients (equation 4) that are independent of measurement settings and small daily changes in alignment of the microscope.

$$N_{corr} = N_{apa} * \left[1 - \frac{I_{autofluorescence}}{I_{total}}\right]^2 * \left[\frac{I_{start}}{I_{ana}}\right] \quad \text{Eq. 3}$$

$$\tau_{diff} = \frac{{\omega_{xy}}^2}{4D} \quad \text{Eq. 4}$$

$$V = 2\pi {\omega_{xy}}^3 * sp \quad \text{Eq. 5}$$

$$C = \frac{N_{corr}}{V * N_A} \quad \text{Eq. 6}$$

The model to fit SGFP2-CTNNB1 measurements contained 2 diffusion components. The first diffusion component was fixed to the speed of monomeric SGFP2-CTNNB1. To estimate the speed of monomeric SGFP2-CTNNB1, the speed of free floating SGFP2, transfected in HAP1 cells, was measured to be 24.1 $\mu m^2 s^{-1}$ using FCS. Subsequently, this speed was used to calculate the speed of monomeric SGFP2-CTNNB1 with Einstein-Stokes formula (Equation 7). As the temperature (T), dynamic viscosity (η) and Boltzmann's constant (k_B) are equal between SGFP2 and SGFP2-CTNNB1 measurements, the expected difference in diffusion speed is only caused by the radius (r) of the diffusing molecule. The difference in radius was approximated by the cubic root of the ratio of the molecular weight of the SGFP2-CTNNB1 fusion protein (88 + 27=115 kDa) and the size of the SGFP2 protein (27 kDa), thus expecting a 1.62 times lower diffusion coefficient (compared to free floating SGFP2) of 14.9 $\mu m^2 s^{-1}$ for SGFP2-CTNNB1.

$$D = \frac{k_B T}{6\pi\eta r} \quad \text{Eq. 7}$$

In the fitting model, the structural parameter was fixed to the one determined by the Alexa488 measurements of that day. To ensure good fitting, limits were set for other parameters; G_∞ [0.5-1.5], N [0.001, 500], τ_{trip} [$1*10^{-6}$-0.05 ms], τ_{diff2} [10-200 ms].

N&B data acquisition and analysis

For N&B analysis, 50 images were acquired per measurement with a pixel time of 100 µs/pixel and a pixel size of 0.138-0.207 µm. The fluorescent signal was acquired with the APD described above for the FCS measurements. As a control and to optimize acquisition settings, HAP1 cells transfected with SGFP2, EGFP monomer or dimer were measured alongside HAP1$^{SGFP2\text{-}CTNNB1}$ cells treated with BSA or WNT3A. APD readout was converted to a TIF stack using a custom build *.ptu* converter (Crosby et al., 2013). This TIF stack was further analyzed using an ImageJ macro script (modified from (Crosby et al., 2013), made available at https://osf.io/ys5qw/) based on Digman, Dalal, Horwitz, & Gratton, 2008.

Within the script, average brightness and particle numbers were calculated for nuclear or cytoplasmic ROIs, which were set based on transmission image. Static or slow-moving particles, including membrane regions, were excluded by thresholding and/or ROI selection, since they can severely impact the brightness measured.

Data representation and statistical analysis

Data processing and representation were performed in RStudio (version 1.1.456 running R 3.5.1 or 3.6.1). 95% confidence intervals of the median mentioned in the text and shown in Table 1-2 were calculated using PlotsOfDifferences (Goedhart, 2019). Representation of the imaging data in Figure 4 supplement 2 and in supplementary movies 3-4 were generated in RStudio using a script based on PlotsOfDifferences (made available at https://osf.io/sxakf/).

Model description

We developed a minimal model for WNT signaling based on a previous model from the Kirschner group (Lee et al., 2003). The R source code of the model is available at https://osf.io/2e8by/.

888 Our minimal model comprises the following reactions:

$CB + DC \underset{k1}{\overset{k2}{\leftrightharpoons}} CB^* - DC$	Binding of cytoplasmic CTNNB1 (CB) to destruction complex	(1)
$CB^* - DC \overset{k3}{\rightarrow} DC + CB^*$	Release of phosphorylated CB (CB*) and recycling of the destruction complex	(2)
$DVL + DC \underset{k4}{\overset{k5}{\leftrightharpoons}} \mathrm{DC}^*$	Inactivation of the destruction complex by DVL	(3)
$CB \underset{k6}{\overset{k7}{\leftrightharpoons}} NB$	Nucleocytoplasmic shuttling of CB to and from the nucleus	(4)
$NB + TCF \underset{k8}{\overset{k9}{\leftrightharpoons}} NB - TCF$	Binding of NB to TCF	(5)

889 Below, we show the differential equations that govern the concentrations of the different
890 compounds over time for the reactions described above. Table 3 in the main text gives the
891 correspondence between the variables (i.e. x_1) in the differential equations and the model
892 name (i.e. CB) in the reactions. The parameter w in equations (7) and (8) is $w = 0$ in the
893 absence of WNT and $w = 1$ if WNT is present, i.e. in our minimal model the inactive form of
894 the destruction complex (DC*) is only present if WNT is present. The parameter b in equation
895 (6) represents the constant production of CTNNB1, corresponding to v_{12} in Lee et al., 2003.

$$\frac{dx_1}{dt} = -k_1 x_1 x_2 + k_2 x_3 - k_6 x_1 + k_7 x_6 + b \quad (6)$$

$$\frac{dx_2}{dt} = -k_1 x_1 x_2 + (k_2 + k_3) x_3 - w(k_4 x_2 - k_5 x_4) \quad (7)$$

$$\frac{dx_3}{dt} = k_1 x_1 x_2 - (k_2 + k_3) x_3 \quad (8)$$

$$\frac{dx_4}{dt} = w(k_4 x_2 - k_5 x_4) \quad (9)$$

$$\frac{dx_5}{dt} = k_6 x_1 - k_7 x_5 - k_8 x_5 x_6 + k_9 x_7 \quad (10)$$

$$\frac{dx_6}{dt} = -k_8 x_5 x_6 + k_9 x_7 \quad (11)$$

$$\frac{dx_7}{dt} = k_8 x_5 x_6 - k_9 x_7 \quad (12)$$

896

Equilibrium conditions without WNT

The parameters in our model can in part be determined from our measurements of the equilibrium concentrations of CB, NB and their complexes, see Table 3-4 in the main text. Where we could not determine the parameters from our measurements, we used published values as indicated.

Under equilibrium conditions, the concentrations of the compounds do not change with time and the left-hand side of equations (6) - (12) is zero. From equations (10) and (11) we can determine the ratio of the rate constants k_6 and k_7 from the measured values of x_1 and x_5:

$$k_6 x_1 = k_7 x_5 \Leftrightarrow \frac{k_6}{k_7} = \frac{x_5}{x_1} = \frac{95}{104} = 0.913 \quad (13)$$

From equations (6), (8), (10) and (11) we have:

$$-k_3 x_3 + b = 0 \Leftrightarrow k_3 = \frac{b}{x_3} = \frac{0.423}{67} = 0.0063 \quad (14)$$

Our reaction (1) corresponds closely to step 8 in Lee et al. therefore, we use the value of the dissociation constant $K_8 = 120$ nM from Lee et al. for our dissociation constant $K_1 = \frac{k_2}{k_1}$.

To calculate the dissociation constant for the NB-TCF complex, we estimate an equilibrium concentration for free TCF (x_6) from Tan et al. (2012). From their Figure 11 it is seen that the bound TCF concentration in equilibrium in the presence of WNT has about the same value as the initial free TCF concentration and that no initial bound TCF is present. However, we measured NB-TCF also in the initial state. Therefore, we consider the free TCF concentration value from Tan et al. as a lower bound for the estimate of total TCF. Also, from Figure 11 of Tan et al. (2012) we estimate that of the initial free TCF, a fifth remains in the nucleus as free TCF after WNT is turned on. We measured 102 nM NB-TCF in the nucleus after the application of WNT. This leads to an estimate of the total concentration of TCF, TCF^0, in the nucleus of:

$[TCF^0] = 102 + 0.2 \times 102 = 122\,\mathrm{nM}$. If we assume that the total TCF concentration does not change by the application of WNT, we calculate the dissociation constant of the NB-TCF complex from equation (12):

$$k_8 x_5 (TCF^0 - x_7) = k_9 x_7 \Rightarrow \frac{k_9}{k_8} = K_2 = \frac{x_5 (TCF^0 - x_7)}{x_7} = \frac{95 * 99}{23} = 409 \qquad (15)$$

Equilibrium conditions with WNT

We model the action of WNT by deactivation of the destruction complex by DVL through reaction 3 by setting $w = 1$ in equations (7) and (9). The dissociation constant of CB*-DC, K_1, is assumed not to change in the presence of WNT. The measurements of free CB and NB in equilibrium (see Table 2) give for the ratio of k_6 and k_7:

$$k_6 x_1 = k_7 x_5 \Leftrightarrow \frac{k_6}{k_7} = \frac{x_5}{x_1} = \frac{186}{145} = 1.28 \qquad (16)$$

The value of the rate of decay of the phosphorylated complex CB*-DC, k_3, is found to be the same for the "without WNT" situation:

$$-k_3 x_3 + b = 0 \Leftrightarrow k_3 = \frac{b}{x_3} = \frac{0.423}{67} = 0.0063 \qquad (17)$$

To uniquely determine the ratio of k_4 and k_5, we need the concentrations of the destruction complex DC and DC$*$ neither of which we have access to. We can, however, fit this ratio with our model to the measured values of x_1 and x_7 and find $k_4/k_5 = 2.56$.

We again calculate the dissociation constant of the NB-TCF complex from equation (12), using the concentrations for NB and NB-TCF obtained with FCS.

$$k_8 x_5 (TCF^0 - x_7) = k_9 x_7 \Rightarrow \frac{k_9}{k_8} = K_2 = \frac{x_5 (TCF^0 - x_7)}{x_7} = \frac{186 * 20}{102} = 36.5 \qquad (18)$$

933 Notice that we determined the ratios of the rate constants from the measured equilibrium
934 values of free and bound CTNNB1 in the cytoplasm and the nucleus. This means that our rate
935 constants are determined up to a multiplicative factor: the equilibrium equations do not
936 change if all rate constants k_i and the parameter b are multiplied by the same factor, R. The
937 factor R determines the rate at which our model system reaches equilibrium. By comparing
938 the times equilibrium was reached by the cytoplasmic and nuclear SGFP2-CTNNB1 signals
939 (Figure 4 C, D) of about 4.5 hours, we fitted a factor $R = 20$ for our model.

940

Acknowledgements

We thank the van Leeuwenhoek Centre for Advanced Microscopy (LCAM, Section Molecular Cytology, Swammerdam Institute for Life Sciences, University of Amsterdam) for the use of their facilities and LCAM staff for sharing their expertise and providing technical support, Jasmijn Span for cloning the color variants of the repair plasmid as a student in our lab, Marten Postma and Joachim Goedhart for assistance with data handling and analysis, Dorus Gadella and Tanne van der Wal for carefully reading the manuscript, and all colleagues for stimulating discussions and suggestions.

This work was funded by a MacGillavry fellowship (University of Amsterdam, to RvA), KWF Kankerbestrijding (career development award ANW 2013-6057 and KWF/Alpe d'HuZes project grant UVA 2015-8014, to RvA), and the Dutch Research Council (NWO VIDI grant 864.13.002 and OCENW.KLEIN.169, to RvA).

Competing interest statement

The authors have no competing interests to declare.

References

Aberle, H., Bauer, A., Stappert, J., Kispert, A., & Kemler, R. (1997). β-catenin is a target for the ubiquitin-proteasome pathway. *The EMBO Journal*, *16*(13), 3797–3804.

Amit, S., Hatzubai, A., Birman, Y., Andersen, J. S., Ben-shushan, E., Mann, M., … Alkalay, I. (2002). Axin-mediated CKI phosphorylation of β-catenin at Ser 45: a molecular switch for the Wnt pathway. *Genes & Development*, *16*, 1066–1076. https://doi.org/10.1101/gad.230302.somal

Andersson, B. S., Beran, M., Pathak, S., Goodacre, A., Barlogie, B., & McCredie, K. B. (1987). Ph-positive chronic myeloid leukemia with near-haploid conversion in vivo and establishment of a continuously growing cell line with similar cytogenetic pattern. *Cancer Genetics and Cytogenetics*, *24*(2), 335–343. https://doi.org/10.1016/0165-4608(87)90116-6

Armstrong, N. J., Fagotto, F., Prothmann, C., & Rupp, R. A. W. (2012). Maternal Wnt/β-catenin signaling coactivates transcription through NF-κB binding sites during xenopus axis formation. *PLoS ONE*, *7*(5). https://doi.org/10.1371/journal.pone.0036136

Bain, J., Plater, L., Elliott, M., Shpiro, N., Hastie, C. J., Mclauchlan, H., … Cohen, P. (2007). The selectivity of protein kinase inhibitors: A further update. *Biochemical Journal*, *408*(3), 297–315. https://doi.org/10.1042/BJ20070797

Barker, N., van Es, J. H., Kuipers, J., Kujala, P., van den Born, M., Cozijnsen, M., … Clevers, H. (2007). Identification of stem cells in small intestine and colon by marker gene Lgr5. *Nature*, *449*(7165), 1003–1007. https://doi.org/10.1038/nature06196

Behrens, J., von Kries, J. P., Kühl, M., Bruhn, L., Wedlich, D., Grosschedl, R., & Birchmeier, W.

(1996). Functional interaction of beta-catenin with the transcription factor LEF-1. *Nature*. https://doi.org/10.1038/382638a0

Benham-Pyle, B. W., Pruitt, B. L., & Nelson, W. J. (2015). Mechanical strain induces E-cadherin-dependent Yap1 and β-catenin activation to drive cell cycle entry. *Science*, *348*(6238), 1024–1027. https://doi.org/10.1126/science.aaa4559

Benham-Pyle, B. W., Sim, J. Y., Hart, K. C., Pruitt, B. L., & Nelson, W. J. (2016). Increasing β-catenin/Wnt3A activity levels drive mechanical strain-induced cell cycle progression through mitosis. *ELife*, *5*(OCTOBER2016), 1–28. https://doi.org/10.7554/eLife.19799

Bilic, J., Huang, Y.-L., Davidson, G., Zimmermann, T., Cruciat, C.-M. C.-M., Bienz, M., & Niehrs, C. (2007). Wnt induces LRP6 signalosomes and promotes dishevelled-dependent LRP6 phosphorylation. *Science (New York, N.Y.)*, *316*(5831), 1619–1622. https://doi.org/10.1126/science.1137065

Bindels, D. S., Haarbosch, L., van Weeren, L., Postma, M., Wiese, K. E., Mastop, M., … Gadella Jr, T. W. J. (2017). mScarlet: a bright monomeric red fluorescent protein for cellular imaging. *Nature Methods*, *14*(1), 53–56. https://doi.org/10.1038/nmeth.4074

Bryja, V., Červenka, I., & Čajánek, L. (2017). The connections of Wnt pathway components with cell cycle and centrosome: side effects or a hidden logic? *Critical Reviews in Biochemistry and Molecular Biology*. https://doi.org/10.1080/10409238.2017.1350135

Canaj, H., Hussmann, J. A., Li, H., Beckman, K. A., Goodrich, L., Cho, Nathan, H., … Leonetti, M. D. (2019). Deep profiling reveals substantial heterogeneity of integration outcomes in CRISPR knock-in experiments. *BioRxiv*. https://doi.org/10.1101/841098

Cantù, C., Felker, A., Zimmerli, D., Prummel, K. D., Cabello, E. M., Chiavacci, E., … Mosimann,

1000 C. (2018). Mutations in Bcl9 and Pygo genes cause congenital heart defects by tissue-
1001 specific perturbation of Wnt/β-catenin signaling. *Genes and Development*, *32*(21–22),
1002 1443–1458. https://doi.org/10.1101/gad.315531.118

1003 Carette, J. E., Raaben, M., Wong, A. C., Herbert, A. S., Obernosterer, G., Mulherkar, N., …
1004 Brummelkamp, T. R. (2011). Ebola virus entry requires the cholesterol transporter
1005 Niemann-Pick C1. *Nature*, *477*(7364), 340–343. https://doi.org/10.1038/nature10348

1006 Chhabra, S., Liu, L., Goh, R., Kong, X., & Warmflash, A. (2019). Dissecting the dynamics of
1007 signaling events in the BMP, WNT, and NODAL cascade during self-organized fate
1008 patterning in human gastruloids. *PLOS Biology*, *17*(10), e3000498.
1009 https://doi.org/10.1371/journal.pbio.3000498

1010 Crosby, K. C., Postma, M., Hink, M. A., Zeelenberg, C. H. C., Adjobo-Hermans, M. J. W., &
1011 Gadella, T. W. J. (2013). Quantitative analysis of self-association and mobility of
1012 Annexin A4 at the plasma membrane. *Biophysical Journal*, *104*(9), 1875–1885.
1013 https://doi.org/10.1016/j.bpj.2013.02.057

1014 Digman, M. A., Dalal, R., Horwitz, A. F., & Gratton, E. (2008). Mapping the number of
1015 molecules and brightness in the laser scanning microscope. *Biophysical Journal*, *94*(6),
1016 2320–2332. https://doi.org/10.1529/biophysj.107.114645

1017 Doumpas, N., Lampart, F., Robinson, M. D., Lentini, A., Nestor, C. E., Cantù, C., & Basler, K.
1018 (2019). TCF / LEF dependent and independent transcriptional regulation of Wnt/β-
1019 catenin target genes . *The EMBO Journal*, *38*(2), 1–14.
1020 https://doi.org/10.15252/embj.201798873

1021 Dross, N., Spriet, C., Zwerger, M., Müller, G., Waldeck, W., & Langowski, J. (2009). Mapping

1022 eGFP oligomer mobility in living cell nuclei. *PLoS ONE*, *4*(4), 1–13.
1023 https://doi.org/10.1371/journal.pone.0005041

1024 Eckert, A. F., Gao, P., Wesslowski, J., Wang, X., Rath, J., Nienhaus, K., … Nienhaus, G. U.
1025 (2020). Measuring ligand-cell surface receptor affinities with axial line-scanning
1026 fluorescence correlation spectroscopy. *ELife*, *9*. https://doi.org/10.7554/eLife.55286

1027 Elson, E. L. (2011). Fluorescence correlation spectroscopy: Past, present, future. *Biophysical*
1028 *Journal*, *101*(12), 2855–2870. https://doi.org/10.1016/j.bpj.2011.11.012

1029 Essers, M. A. G. G., De Vries-Smits, L. M. M. M., Barker, N., Polderman, P. E., Burgering, B. M.
1030 T. T., & Korswagen, H. C. (2005). Functional interaction between β-catenin and FOXO in
1031 oxidative stress signaling. *Science*, *308*(5725), 1181–1184.
1032 https://doi.org/10.1126/science.1109083

1033 Essletzbichler, P., Konopka, T., Santoro, F., Chen, D., Gapp, B. V., Kralovics, R., …
1034 Bürckstümmer, T. (2014). Megabase-scale deletion using CRISPR/Cas9 to generate a
1035 fully haploid human cell line. *Genome Research*, *24*(12), 2059–2065.
1036 https://doi.org/10.1101/gr.177220.114

1037 Fagotto, F. (2013, April 19). Looking beyond the Wnt pathway for the deep nature of β-
1038 catenin. *EMBO Reports*. John Wiley & Sons, Ltd.
1039 https://doi.org/10.1038/embor.2013.45

1040 Fagotto, F., Glück, U., & Gumbiner, B. M. (1998). Nuclear localization signal-independent
1041 and importin/karyopherin-independent nuclear import of β-catenin. *Current Biology*,
1042 *8*(4), 181–190. https://doi.org/10.1016/S0960-9822(98)70082-X

1043 Fagotto, F., Jho, E. H., Zeng, L., Kurth, T., Joos, T., Kaufmann, C., & Costantini, F. (1999).

1044 Domains of Axin involved in protein-protein interactions, Wnt pathway inhibition, and
1045 intracellular localization. *Journal of Cell Biology*, *145*(4), 741–756.
1046 https://doi.org/10.1083/jcb.145.4.741

1047 Faux, M. C., Coates, J. L., Catimel, B., Cody, S., Clayton, A. H. A., Layton, M. J., & Burgess, A.
1048 W. (2008). Recruitment of adenomatous polyposis coli and beta-catenin to axin-puncta.
1049 *Oncogene*, *27*(44), 5808–5820. https://doi.org/10.1038/onc.2008.205

1050 Fiedler, M., Graeb, M., Mieszczanek, J., Rutherford, T. J., Johnson, C. M., & Bienz, M. (2015).
1051 An ancient Pygo-dependent Wnt enhanceosome integrated by chip/LDB-SSDP. *ELife*,
1052 *4*(AUGUST2015), 1–22. https://doi.org/10.7554/eLife.09073

1053 Fiedler, M., Mendoza-Topaz, C., Rutherford, T. J., Mieszczanek, J., & Bienz, M. (2011).
1054 Dishevelled interacts with the DIX domain polymerization interface of Axin to interfere
1055 with its function in down-regulating β-catenin. *Proceedings of the National Academy of*
1056 *Sciences of the United States of America*, *108*(5), 1937–1942.
1057 https://doi.org/10.1073/pnas.1017063108

1058 Franz, A., Shlyueva, D., Brunner, E., Stark, A., & Basler, K. (2017). Probing the canonicity of
1059 the Wnt/Wingless signaling pathway. *PLoS Genetics*, *13*(4), 1–18.
1060 https://doi.org/10.1371/journal.pgen.1006700

1061 Fuerer, C., Nostro, M. C., & Constam, D. B. (2014). Nodal·Gdf1 heterodimers with bound
1062 prodomains enable serum-independent nodal signaling and endoderm differentiation.
1063 *Journal of Biological Chemistry*, *289*(25), 17854–17871.
1064 https://doi.org/10.1074/jbc.M114.550301

1065 Gammons, M., & Bienz, M. (2018). Multiprotein complexes governing Wnt signal

transduction. *Current Opinion in Cell Biology*, *51*, 42–49. https://doi.org/10.1016/j.ceb.2017.10.008

Gayrard, C., Bernaudin, C., Déjardin, T., Seiler, C., & Borghi, N. (2018). Src- and confinement-dependent FAK activation causes E-cadherin relaxation and β-catenin activity. *Journal of Cell Biology*, *217*(3), 1063–1077. https://doi.org/10.1083/jcb.201706013

Gerlach, J. P., Emmink, B. L., Nojima, H., Kranenburg, O., & Maurice, M. M. (2014). Wnt signalling induces accumulation of phosphorylated β-catenin in two distinct cytosolic complexes. *Open Biology*, *4*(11), 140120. https://doi.org/10.1098/rsob.140120

Gibson, D. G., Young, L., Chuang, R. Y., Venter, J. C., Hutchison, C. A., & Smith, H. O. (2009). Enzymatic assembly of DNA molecules up to several hundred kilobases. *Nature Methods*, *6*(5), 343–345. https://doi.org/10.1038/nmeth.1318

Gibson, T. J., Seiler, M., & Veitia, R. A. (2013). The transience of transient overexpression. *Nature Methods*, *10*(8), 715–721. https://doi.org/10.1038/nmeth.2534

Goedhart, J. (2019). PlotsOfDifferences - a web app for the quantitative comparison of unpaired data. *BioRxiv*, 578575. https://doi.org/10.1101/578575

Goedhart, J., von Stetten, D., Noirclerc-Savoye, M., Lelimousin, M., Joosen, L., Hink, M. A., … Royant, A. (2012). Structure-guided evolution of cyan fluorescent proteins towards a quantum yield of 93%. *Nature Communications*. https://doi.org/10.1038/ncomms1738

Gottardi, C. J., & Gumbiner, B. M. (2004). Distinct molecular forms of β-catenin are targeted to adhesive or transcriptional complexes. *Journal of Cell Biology*, *167*(2), 339–349. https://doi.org/10.1083/jcb.200402153

Hampf, M., & Gossen, M. (2006). A protocol for combined Photinus and Renilla luciferase

quantification compatible with protein assays. *Analytical Biochemistry*, *356*(1), 94–99. https://doi.org/10.1016/j.ab.2006.04.046

Hendriksen, J., Jansen, M., Brown, C. M., van der Velde, H., van Ham, M., Galjart, N., … Fornerod, M. (2008). Plasma membrane recruitment of dephosphorylated β-catenin upon activation of the Wnt pathway. *Journal of Cell Science*, *121*(11), 1793–1802. https://doi.org/10.1242/jcs.025536

Hink, M. a. (2014). Quantifying intracellular dynamics using fluorescence fluctuation spectroscopy. *Protoplasma*, *251*(2), 307–316. https://doi.org/10.1007/s00709-013-0602-z

Holstein, T. W. (2012). The evolution of the wnt pathway. *Cold Spring Harbor Perspectives in Biology*, *4*(7), 1–17. https://doi.org/10.1101/cshperspect.a007922

Holzmann, J., Politi, A. Z., Nagasaka, K., Hantsche-Grininger, M., Walther, N., Koch, B., … Peters, J.-M. (2019). Absolute quantification of cohesin, CTCF and their regulators in human cells. *ELife*, *8*, 1–31. https://doi.org/10.7554/elife.46269

Howard, S., Deroo, T., Fujita, Y., & Itasaki, N. (2011). A positive role of cadherin in Wnt/β-catenin signalling during epithelial-mesenchymal transition. *PloS One*, *6*(8), e23899. https://doi.org/10.1371/journal.pone.0023899

Hu, M., Kurobe, M., Jeong, Y. J., Fuerer, C., Ghole, S., Nusse, R., & Sylvester, K. G. (2007). Wnt/β-catenin signaling in murine hepatic transit amplifying progenitor cells. *Gastroenterology*, *133*(5), 1579–1591. https://doi.org/10.1053/j.gastro.2007.08.036

Jacobsen, A., Heijmans, N., Verkaar, F., Smit, M. J., Heringa, J., van Amerongen, R., & Feenstra, K. A. (2016). Construction and experimental validation of a Petri net model of

Wnt/β-catenin signaling. *PLoS ONE*, *11*(5), 1–30. https://doi.org/10.1101/044966

Jamieson, C., Sharma, M., & Henderson, B. R. (2011). Regulation of β-catenin nuclear dynamics by GSK-3β involves a LEF-1 positive feedback loop. *Traffic*, *12*(8), 983–999. https://doi.org/10.1111/j.1600-0854.2011.01207.x

Kafri, P., Hasenson, S. E., Kanter, I., Sheinberger, J., Kinor, N., Yunger, S., & Shav-Tal, Y. (2016). Quantifying β-catenin subcellular dynamics and cyclin D1 mRNA transcription during Wnt signaling in single living cells. *ELife*, *5*(NOVEMBER2016), 1–29. https://doi.org/10.7554/eLife.16748

Kaur, G., Costa, M. W., Nefzger, C. M., Silva, J., Fierro-González, J. C., Polo, J. M., … Plachta, N. (2013). Probing transcription factor diffusion dynamics in the living mammalian embryo with photoactivatable fluorescence correlation spectroscopy. *Nature Communications*, *4*(1), 1637. https://doi.org/10.1038/ncomms2657

Keller, B. M., Maier, J., Secker, K. A., Egetemaier, S. M., Parfyonova, Y., Rothbauer, U., & Traenkle, B. (2018). Chromobodies to quantify changes of endogenous protein concentration in living cells. *Molecular and Cellular Proteomics*, *17*(12), 2518–2533. https://doi.org/10.1074/mcp.TIR118.000914

Kitazawa, M., Hatta, T., Ogawa, K., Fukuda, E., Goshima, N., & Natsume, T. (2017). Determination of rate-limiting factor for formation of beta-catenin destruction complexes using absolute protein quantification. *Journal of Proteome Research*, *16*(10), 3576–3584. https://doi.org/10.1021/acs.jproteome.7b00305

Kormish, J. D., Sinner, D., & Zorn, A. M. (2010). Interactions between SOX factors and Wnt/β-catenin signaling in development and disease. *Developmental Dynamics*, *239*(1),

56–68. https://doi.org/10.1002/dvdy.22046

Kotecki, M., Reddy, P. S. S., & Cochran, B. H. (1999). Isolation and characterization of a near-haploid human cell line. *Experimental Cell Research*, *252*(2), 273–280. https://doi.org/10.1006/excr.1999.4656

Kremers, G.-J., Goedhart, J., van den Heuvel, D. J., Gerritsen, H. C., & Gadella, T. W. J. (2007). Improved green and blue fluorescent proteins for expression in bacteria and mammalian cells. *Biochemistry*, *46*(12), 3775–3783. https://doi.org/10.1021/bi0622874

Kremers, G. J., Goedhart, J., Van Munster, E. B., Gadella, T. W. J. J., Munster, E. B. Van, & Gadella, T. W. J. J. (2006). Cyan and yellow super fluorescent proteins with improved brightness , protein folding , and FRET förster radius. *Biochemistry*, *45*(21), 6570–6580. https://doi.org/10.1021/bi0516273

Krieghoff, E., Behrens, J., & Mayr, B. (2006). Nucleo-cytoplasmic distribution of β-catenin is regulated by retention. *Journal of Cell Science*, *119*(7), 1453–1463. https://doi.org/10.1242/jcs.02864

Kunttas-Tatli, E., Roberts, D. M., & McCartney, B. M. (2014). Self-association of the APC tumor suppressor is required for the assembly, stability, and activity of the Wnt signaling destruction complex. *Molecular Biology of the Cell*, *25*(21), 3424–3436. https://doi.org/10.1091/mbc.E14-04-0885

Lam, C. S., Mistri, T. K., Foo, Y. H., Sudhaharan, T., Gan, H. T., Rodda, D., … Ahmed, S. (2012). DNA-dependent Oct4-Sox2 interaction and diffusion properties characteristic of the pluripotent cell state revealed by fluorescence spectroscopy. *Biochemical Journal*, *448*(1), 21–33. https://doi.org/10.1042/BJ20120725

1154 Latres, E., Chiaur, D. S., & Pagano, M. (1999). The human F box protein β-Trcp associates
1155 with the Cul1/Skp1 complex and regulates the stability of β-catenin. *Oncogene*, *18*(4),
1156 849–854. https://doi.org/10.1038/sj.onc.1202653

1157 Lebensohn, A. A. M., Dubey, R., Neitzel, L. R., Tacchelly-Benites, O., Yang, E., Marceau, C. D.,
1158 … Ahmed, Y. (2016). Comparative genetic screens in human cells reveal new regulatory
1159 mechanisms in WNT signaling. *ELife*, *5*, e21459. https://doi.org/10.7554/eLife.21459

1160 Lee, E., Salic, A., Krüger, R., Heinrich, R., & Kirschner, M. W. (2003). The roles of APC and
1161 axin derived from experimental and theoretical analysis of the Wnt pathway. *PLoS*
1162 *Biology*, *1*(1), 116–132. https://doi.org/10.1371/journal.pbio.0000010

1163 Li, V. S. W., Ng, S. S., Boersema, P. J., Low, T. Y., Karthaus, W. R., Gerlach, J. P., … Clevers, H.
1164 (2012). Wnt signaling through inhibition of β-catenin degradation in an intact Axin1
1165 complex. *Cell*, *149*(6), 1245–1256. https://doi.org/10.1016/j.cell.2012.05.002

1166 Lim, X., Tan, S., Koh, W. W. L. C., Chau, R., Yan, K., Kuo, C. J., … Nusse, R. (2013).
1167 Interfollicular epidermal stem cells self-renew via autocrine Wnt signaling. *Science*,
1168 *342*(December), 1226–1230. https://doi.org/10.1126/science.1239730.Interfollicular

1169 Liu, C., Li, Y., Semenov, M., Han, C., Baeg, G.-H. H., Tan, Y., … He, X. (2002). Control of β-
1170 catenin phosphorylation/degradation by a dual-kinase mechanism. *Cell*, *108*(6), 837–
1171 847. https://doi.org/10.1016/S0092-8674(02)00685-2

1172 Liu, X., Rubin, J. S., & Kimmel, A. R. (2005). Rapid, Wnt-induced changes in GSK3β
1173 associations that regulate β-catenin stabilization are mediated by Gα proteins. *Current*
1174 *Biology*, *15*(22), 1989–1997. https://doi.org/10.1016/j.cub.2005.10.050

1175 Livak, K. J., & Schmittgen, T. D. (2001). Analysis of relative gene expression data using real-

1176 time quantitative PCR and the 2-ΔΔCT method. *Methods*, *25*(4), 402–408.
1177 https://doi.org/10.1006/meth.2001.1262

1178 Loh, K. M., van Amerongen, R., & Nusse, R. (2016). Generating cellular diversity and spatial
1179 form: Wnt signaling and the evolution of multicellular animals. *Developmental Cell*,
1180 *38*(6), 643–655. https://doi.org/10.1016/j.devcel.2016.08.011

1181 Lui, T. T. H., Lacroix, C., Ahmed, S. M., Goldenberg, S. J., Leach, C. A., Daulat, A. M., & Angers,
1182 S. (2011). The ubiquitin-specific protease USP34 regulates Axin stability and Wnt/β-
1183 Catenin Signaling. *Molecular and Cellular Biology*, *31*(10), 2053–2065.
1184 https://doi.org/10.1128/mcb.01094-10

1185 Lustig, B., Jerchow, B., Sachs, M., Weiler, S., Pietsch, T., Karsten, U., … Behrens, J. (2002).
1186 Negative feedback loop of Wnt signaling through upregulation of conductin/axin2 in
1187 colorectal and liver tumors. *Molecular and Cellular Biology*, *22*(4), 1184–1193.
1188 https://doi.org/10.1128/mcb.22.4.1184-1193.2002

1189 Macháň, R., & Wohland, T. (2014). Recent applications of fluorescence correlation
1190 spectroscopy in live systems. *FEBS Letters*, *588*(19), 3571–3584.
1191 https://doi.org/10.1016/j.febslet.2014.03.056

1192 Mahen, R., Koch, B., Wachsmuth, M., Politi, A. Z., Perez-gonzalez, A., Mergenthaler, J., …
1193 Lippincott-schwartz, J. (2014). Comparative assessment of fluorescent transgene
1194 methods for quantitative imaging in human cells. *Molecular Biology of the Cell*, *25*,
1195 3610–3618. https://doi.org/10.1091/mbc.E14-06-1091

1196 Maher, M. T., Mo, R., Flozak, A. S., Peled, O. N., & Gottardi, C. J. (2010). β-Catenin
1197 phosphorylated at Serine 45 is spatially uncoupled from β-Catenin phosphorylated in

1198 the GSK3 domain: Implications for signaling. *PLoS ONE*, *5*(4), e10184.
1199 https://doi.org/10.1371/journal.pone.0010184

1200 Massey, J., Liu, Y., Alvarenga, O., Saez, T., Schmerer, M., & Warmflash, A. (2019). Synergy
1201 with TGFβ ligands switches WNT pathway dynamics from transient to sustained during
1202 human pluripotent cell differentiation. *Proceedings of the National Academy of*
1203 *Sciences of the United States of America*, *116*(11), 4989–4998.
1204 https://doi.org/10.1073/pnas.1815363116

1205 Mendoza-Topaz, C., Mieszczanek, J., & Bienz, M. (2011). The Adenomatous polyposis coli
1206 tumour suppressor is essential for Axin complex assembly and function and opposes
1207 Axin's interaction with Dishevelled. *Open Biology*, *1*(3), 110013.
1208 https://doi.org/10.1098/rsob.110013

1209 Molenaar, M., van de Wetering, M., Oosterwegel, M., Peterson-Maduro, J., Godsave, S.,
1210 Korinek, V., … Clevers, H. (1996). XTcf-3 transcription factor mediates beta-catenin-
1211 induced axis formation in Xenopus embryos. *Cell*, *86*(3), 391–399.
1212 https://doi.org/10.1016/S0092-8674(00)80112-9

1213 Nusse, R., & Clevers, H. (2017). Wnt/β-Catenin signaling, disease, and emerging therapeutic
1214 modalities. *Cell*, *169*(6), 985–999. https://doi.org/10.1016/j.cell.2017.05.016

1215 Olmeda, D., Castel, S., Vilaró, S., & Cano, A. (2003). β-Catenin regulation during the cell
1216 cycle: Implications in G2/M and apoptosis. *Molecular Biology of the Cell*, *14*(7), 2844–
1217 2860. https://doi.org/10.1091/mbc.e03-01-0865

1218 Pack, C. G., Yukii, H., Toh-E, A., Kudo, T., Tsuchiya, H., Kaiho, A., … Saeki, Y. (2014).
1219 Quantitative live-cell imaging reveals spatio-temporal dynamics and cytoplasmic

1220 assembly of the 26S proteasome. *Nature Communications*, *5*(1), 3396.
1221 https://doi.org/10.1038/ncomms4396

1222 Pack, C., Saito, K., Tamura, M., & Kinjo, M. (2006). Microenvironment and effect of energy
1223 depletion in the nucleus analyzed by mobility of multiple oligomeric EGFPs. *Biophysical*
1224 *Journal*, *91*(10), 3921–3936. https://doi.org/10.1529/biophysj.105.079467

1225 Petrášek, Z., & Schwille, P. (2008). Precise measurement of diffusion coefficients using
1226 scanning fluorescence correlation spectroscopy. *Biophysical Journal*, *94*(4), 1437–1448.
1227 https://doi.org/10.1529/biophysj.107.108811

1228 Polakis, P. (2000). Wnt signaling and cancer. *Genes & Development*, *14*(15), 1837–1851.
1229 https://doi.org/10.1038/nature03319

1230 Pronobis, M. I., Deuitch, N., Posham, V., Mimori-Kiyosue, Y., & Peifer, M. (2017).
1231 Reconstituting regulation of the canonical Wnt pathway by engineering a minimal β-
1232 catenin destruction machine. *Molecular Biology of the Cell*, *28*(1), 41–53.
1233 https://doi.org/10.1091/mbc.E16-07-0557

1234 Pronobis, M. I., Rusan, N. M., & Peifer, M. (2015). A novel GSK3-regulated APC:Axin
1235 interaction regulates Wnt signaling by driving a catalytic cycle of efficient βcatenin
1236 destruction. *ELife*, *4*(September 2015), 1–31. https://doi.org/10.7554/eLife.08022

1237 Ran, F. A., Hsu, P. D., Wright, J., Agarwala, V., Scott, D. a, & Zhang, F. (2013). Genome
1238 engineering using the CRISPR-Cas9 system. *Nature Protocols*, *8*(11), 2281–2308.
1239 https://doi.org/10.1038/nprot.2013.143

1240 Rim, E. Y., Kinney, L. K., & Nusse, R. (2020). Beta-catenin-mediated Wnt signal transduction
1241 proceeds through an endocytosis-independent mechanism. *Molecular Biology of the*

Cell, mbc.E20-02-0114. https://doi.org/10.1091/mbc.E20-02-0114

Sayat, R., Leber, B., Grubac, V., Wiltshire, L., & Persad, S. (2008). O-GlcNAc-glycosylation of β-catenin regulates its nuclear localization and transcriptional activity. *Experimental Cell Research*, *314*(15), 2774–2787. https://doi.org/10.1016/j.yexcr.2008.05.017

Schaefer, K. N., Bonello, T. T., Zhang, S., Williams, C. E., Roberts, D. M., McKay, D. J., & Peifer, M. (2018). *Supramolecular assembly of the beta-catenin destruction complex and the effect of Wnt signaling on its localitzation, molecular size, and activity in vivo*. *PLoS Genetics* (Vol. 14). Retrieved from http://journals.plos.org/plosgenetics/article/file?id=10.1371/journal.pgen.1007339&type=printable

Schaefer, K. N., & Peifer, M. (2019). Wnt/beta-catenin signaling regulation and a role for biomolecular condensates. *Developmental Cell*, *48*(4), 429–444. https://doi.org/10.1016/j.devcel.2019.01.025

Schaefer, K. N., Pronobis, M., Williams, C. E., Zhang, S., Bauer, L., Goldfarb, D., … Peifer, M. (2020). Wnt regulation: Exploring Axin-Disheveled interactions and defining mechanisms by which the SCF E3 ubiquitin ligase is recruited to the destruction complex. *Molecular Biology of the Cell*, mbcE19110647. https://doi.org/10.1091/mbc.e19-11-0647

Schmittgen, T. D., & Livak, K. J. (2008). Analyzing real-time PCR data by the comparative CT method. *Nature Protocols*, *3*(6), 1101–1108. https://doi.org/10.1038/nprot.2008.73

Schmitz, Y., Rateitschak, K., & Wolkenhauer, O. (2013). Analysing the impact of nucleo-cytoplasmic shuttling of β-catenin and its antagonists APC, Axin and GSK3 on Wnt/β-

1264 catenin signalling. *Cellular Signalling*, *25*(11), 2210–2221.
1265 https://doi.org/10.1016/j.cellsig.2013.07.005

1266 Schuijers, J., Mokry, M., Hatzis, P., Cuppen, E., & Clevers, H. (2014). Wnt-induced
1267 transcriptional activation is exclusively mediated by TCF/LEF. *EMBO Journal*, *33*(2),
1268 146–156. https://doi.org/10.1002/embj.201385358

1269 Schwarz-Romond, T., Fiedler, M., Shibata, N., Butler, P. J. G., Kikuchi, A., Higuchi, Y., & Bienz,
1270 M. (2007). The DIX domain of Dishevelled confers Wnt signaling by dynamic
1271 polymerization. *Nature Structural and Molecular Biology*, *14*(6), 484–492.
1272 https://doi.org/10.1038/nsmb1247

1273 Spink, K. E., Polakis, P., & Weis, W. I. (2000). Structural basis of the Axin–adenomatous
1274 polyposis coli interaction. *The EMBO Journal*, *19*(10), 2270–2279.
1275 https://doi.org/10.1093/emboj/19.10.2270

1276 Stamos, J. L., Chu, M. L.-H. H., Enos, M. D., Shah, N., & Weis, W. I. (2014). Structural basis of
1277 GSK-3 inhibition by N-terminal phosphorylation and by the Wnt receptor LRP6. *ELife*,
1278 *2014*(3), e01998. https://doi.org/10.7554/eLife.01998

1279 Taelman, V. F., Dobrowolski, R., Plouhinec, J. L., Fuentealba, L. C., Vorwald, P. P., Gumper, I.,
1280 … De Robertis, E. M. (2010). Wnt signaling requires sequestration of Glycogen Synthase
1281 Kinase 3 inside multivesicular endosomes. *Cell*, *143*(7), 1136–1148.
1282 https://doi.org/10.1016/j.cell.2010.11.034

1283 Tan, C. W., Gardiner, B. S., Hirokawa, Y., Layton, M. J., Smith, D. W., & Burgess, A. W. (2012).
1284 Wnt signalling pathway parameters for mammalian cells. *PLoS ONE*, *7*(2), 31882.
1285 https://doi.org/10.1371/journal.pone.0031882

1286 Tan, C. W., Gardiner, B. S., Hirokawa, Y., Smith, D. W., & Burgess, A. W. (2014). Analysis of
1287 Wnt signaling β-catenin spatial dynamics in HEK293T cells. *BMC Systems Biology*, *8*(1),
1288 44. https://doi.org/10.1186/1752-0509-8-44

1289 Thorvaldsen, T. E., Pedersen, N. M., Wenzel, E. M., Schultz, S. W., Brech, A., Liestøl, K., …
1290 Stenmark, H. (2015). Structure, dynamics, and functionality of tankyrase inhibitor-
1291 induced degradasomes. *Molecular Cancer Research*, *13*(11), 1487–1501.
1292 https://doi.org/10.1158/1541-7786.MCR-15-0125

1293 Tortelote, G. G., Reis, R. R., de Almeida Mendes, F., & Abreu, J. G. (2017). Complexity of the
1294 Wnt/β-catenin pathway: Searching for an activation model. *Cellular Signalling*,
1295 *40*(May), 30–43. https://doi.org/10.1016/j.cellsig.2017.08.008

1296 Traenkle, B., Emele, F., Anton, R., Poetz, O., Haeussler, R. S., Maier, J., … Rothbauer, U.
1297 (2015). Monitoring interactions and dynamics of endogenous beta-catenin with
1298 intracellular nanobodies in living cells. *Molecular & Cellular Proteomics*, *14*(3), 707–723.
1299 https://doi.org/10.1074/mcp.M114.044016

1300 Tran, H., & Polakis, P. (2012). Reversible modification of adenomatous polyposis coli (APC)
1301 with K63-linked polyubiquitin regulates the assembly and activity of the β-catenin
1302 destruction complex. *Journal of Biological Chemistry*, *287*(34), 28552–28563.
1303 https://doi.org/10.1074/jbc.M112.387878

1304 Valenta, T., Hausmann, G., & Basler, K. (2012). The many faces and functions of β-catenin.
1305 *The EMBO Journal*, *31*(12), 2714–2736. https://doi.org/10.1038/emboj.2012.150

1306 van Amerongen, R., Bowman, A. N., & Nusse, R. (2012). Developmental stage and time
1307 dictate the fate of Wnt/β-catenin-responsive stem cells in the mammary gland. *Cell*

Stem Cell, *11*(3), 387–400. https://doi.org/10.1016/j.stem.2012.05.023

van Amerongen, R., & Nusse, R. (2009). Towards an integrated view of Wnt signaling in development. *Development*, *136*(19), 3205–3214. https://doi.org/10.1242/dev.033910

van Leeuwen, I. M. M., Byrne, H. M., Jensen, O. E., & King, J. R. (2007). Elucidating the interactions between the adhesive and transcriptional functions of β-catenin in normal and cancerous cells. *Journal of Theoretical Biology*, *247*(1), 77–102. https://doi.org/10.1016/j.jtbi.2007.01.019

van Tienen, L. M., Mieszczanek, J., Fiedler, M., Rutherford, T. J., & Bienz, M. (2017). Constitutive scaffolding of multiple Wnt enhanceosome components by legless/BCL9. *ELife*, *6*, 1–23. https://doi.org/10.7554/eLife.20882

Wachsmuth, M., Waldeck, W., & Langowski, J. (2000). Anomalous diffusion of fluorescent probes inside living cell investigated by spatially-resolved fluorescence correlation spectroscopy. *Journal of Molecular Biology*, *298*(4), 677–689. https://doi.org/10.1006/jmbi.2000.3692

Wiechens, N., & Fagotto, F. (2001). CRM1- and Ran-independent nuclear export of β-catenin. *Current Biology*, *11*(1), 18–28. https://doi.org/10.1016/S0960-9822(00)00045-2

Wiese, K. E., Nusse, R., & van Amerongen, R. (2018). Wnt signalling: conquering complexity. *Development*, *145*(12), dev165902. https://doi.org/10.1242/dev.165902

Wu, X., Tu, X., Joeng, K. S., Hilton, M. J., Williams, D. A., & Long, F. (2008). Rac1 Activation Controls Nuclear Localization of β-catenin during Canonical Wnt Signaling. *Cell*, *133*(2), 340–353. https://doi.org/10.1016/j.cell.2008.01.052

1330 Yaguchi, K., Yamamoto, T., Matsui, R., Tsukada, Y., Shibanuma, A., Kamimura, K., … Uehara,
1331 R. (2018). Uncoordinated centrosome cycle underlies the instability of non-diploid
1332 somatic cells in mammals. *The Journal of Cell Biology*, *217*(7), 2463–2483.
1333 https://doi.org/10.1083/jcb.201701151

1334 Yap, A. S., Brieher, W. M., & Gumbiner, B. M. (1997). Molecular and functional analysis of
1335 cadherin-based adherens junctions. *Annual Review of Cell and Developmental Biology*,
1336 *13*(1), 119–146. https://doi.org/10.1146/annurev.cellbio.13.1.119

1337 Yokoya, F., Imamoto, N., Tachibana, T., & Yoneda, Y. (1999). β-Catenin can be transported
1338 into the nucleus in a ran-unassisted manner. *Molecular Biology of the Cell*, *10*(4), 1119–
1339 1131. https://doi.org/10.1091/mbc.10.4.1119

1340 Yokoyama, N., Markova, N. G., Wang, H., & Malbon, C. C. (2012). Assembly of Dishevelled 3-
1341 based supermolecular complexes via phosphorylation and Axin. *Journal of Molecular*
1342 *Signaling*, *7*(0), 8. https://doi.org/10.1186/1750-2187-7-8

1343 Zhan, T., Rindtorff, N., & Boutros, M. (2017). Wnt signaling in cancer. *Oncogene*, *36*(11),
1344 1461–1473. https://doi.org/10.1038/onc.2016.304

1345

Supplementary Movie legends

Supplementary Movie 1-3: Representative movies of confocal time-lapse experiments, showing SGFP2-CTNNB1 (left, green), SiR-DNA staining (middle, magenta) and transmission image (right, grey) after treatment with vehicle control (BSA) (**Supplementary Movie 1**), 100 ng/ml WNT3A (**Supplementary Movie 2**) or 8 µM CHIR99021 (**Supplementary Movie 3**). Time of addition is at 00:00:00 (indicated at the top left). Scale bar in the lower right represents 20µm.

Supplementary Movie 4-6: Movies showing the quantification of time-lapse microscopy series (from Figure 4 and Supplementary Movie 1-3) at each time point showing all individual cells from 3 biological experiments. Time of addition of the indicated substances is at 00:00:00 (indicated at the top left). The left graph represents the raw data (colored dots, each dot is one cell, n=155-400 cells for each condition and time point), the median (black circle) and the 95% CI of the median (black bar). The right graph represents the median difference (black circle) from the treatments to the control (BSA). When the 95% CI (black bar) does not overlap 0, the difference between the two conditions is significant.

Supplementary Movie 4: Quantification of the normalized intensity of SGFP2-CTNNB1 in the cytoplasm. Significant changes in intensity can first be observed after 40 minutes of 8 µM CHIR99021, and after 70-80 minutes of 4 µM CHIR99021 or 25-100ng/ml WNT3A treatment.

Supplementary Movie 5: Quantification of the normalized intensity of SGFP2-CTNNB1 in the nucleus. Significant changes in intensity can be observed for all treatments (but not controls) after 20-50 minutes.

Supplementary Movie 6: Quantification of the nuclear-cytoplasmic ratio of SGFP2-CTNNB1, calculated from raw intensity values underlying Supplementary Movies 4 and 5. Significant changes in the nuclear-cytoplasmic ratio can be observed for all treatments (but not controls) after 20-50 minutes.